











# Oxygen abundances in the narrow line regions of Seyfert galaxies and the metallicity–luminosity relation

Mark Armah <sup>1</sup>★, Rogério Riffel <sup>1,2</sup>★, O. L. Dors <sup>3</sup>, Kyuseok Oh <sup>4,5</sup>, Michael J. Koss <sup>6,7</sup>,  
Claudio Ricci <sup>8,9</sup>, Benny Trakhtenbrot <sup>10</sup>, Mabel Valerdi <sup>11</sup>, Rogemar A. Riffel <sup>2,12</sup>  
and Angela C. Krabbe <sup>3</sup>

<sup>1</sup>Departamento de Astronomia, Instituto de Física, Universidade Federal do Rio Grande do Sul, CP 15051, 91501-970 Porto Alegre, RS, Brazil

<sup>2</sup>Laboratório Interinstitucional de e-Astronomia - LIneA, Rua General José Cristino 77, Rio de Janeiro, RJ - 20921-400, Brazil

<sup>3</sup>Universidade do Vale do Paraíba. Av. Shishima Hifumi, 2911, CEP: 12244-000, São José dos Campos, SP, Brazil

<sup>4</sup>Korea Astronomy and Space Science Institute, Daedeokdae-ro 776, Yuseong-gu, Daejeon 34055, Republic of Korea

<sup>5</sup>Department of Astronomy, Kyoto University, Kitashirakawa-Oiwake-cho, Sakyo-ku, Kyoto 606-8502, Japan

<sup>6</sup>Eureka Scientific, 2452 Delmer Street Suite 100, Oakland, CA 94602-3017, USA

<sup>7</sup>Space Science Institute, 4750 Walnut Street, Suite 205, Boulder, Colorado 80301, USA

<sup>8</sup>Núcleo de Astronomía de la Facultad de Ingeniería, Universidad Diego Portales, Av. Ejército Libertador 441, Santiago 22, Chile

<sup>9</sup>Kavli Institute for Astronomy and Astrophysics, Peking University, Beijing 100871, People's Republic of China

<sup>10</sup>School of Physics and Astronomy, Tel Aviv University, Tel Aviv 69978, Israel

<sup>11</sup>Instituto Nacional de Astrofísica, Óptica y Electrónica (INAOE), Luis E. Erro No. 1, Sta. Ma. Tonantzintla, Puebla, C.P. 72840, México

<sup>12</sup>Departamento de Física, CCNE, Universidade Federal de Santa Maria, 97105-900 Santa Maria, RS, Brazil

Accepted 2023 January 18. Received 2023 January 4; in original form 2022 November 9

## ABSTRACT

We present oxygen abundances relative to hydrogen (O/H) in the narrow line regions (NLRs) gas phases of Seyferts 1 (Sy 1s) and Seyferts 2 (Sy 2s) active galactic nuclei (AGNs). We used fluxes of the optical narrow emission line intensities [ $3\,500 < \lambda(\text{Å}) < 7\,000$ ] of 561 Seyfert nuclei in the local Universe ( $z \lesssim 0.31$ ) from the second catalogue and data release (DR2) of the BAT AGN Spectroscopic Survey, which focuses on the *Swift*-BAT hard X-ray ( $\gtrsim 10$  keV) detected AGNs. We derived O/H from relative intensities of the emission lines via the strong-line methods. We find that the AGN O/H abundances are related to their hosts stellar masses and that they follow a downward redshift evolution. The derived O/H together with the hard X-ray luminosity ( $L_X$ ) were used to study the X-ray luminosity–metallicity ( $L_X$ – $Z_{\text{NLR}}$ ) relation for the first time in Seyfert galaxies. In contrast to the broad-line focused ( $L_X$ – $Z_{\text{BLR}}$ ) studies, we find that the  $L_X$ – $Z_{\text{NLR}}$  exhibit significant anticorrelations with the Eddington ratio ( $\lambda_{\text{Edd}}$ ) and these correlations vary with redshifts. This result indicates that the low-luminous AGNs are more actively undergoing interstellar medium enrichment through star formation in comparison with the more luminous X-ray sources. Our results suggest that the AGN is somehow driving the galaxy chemical enrichment, as a result of the inflow of pristine gas that is diluting the metal rich gas, together with a recent cessation on the circumnuclear star-formation.

**Key words:** galaxies: abundances – galaxies: active – galaxies: evolution – galaxies: formation – galaxies: ISM – galaxies: Seyfert.

## 1 INTRODUCTION

There are significant observational data which point to a direct link between the host galaxies and the accretion onto supermassive black holes (SMBHs). For instance, the masses of star bulges and the masses of their central SMBHs are tightly correlated (see Kormendy & Ho 2013; Graham 2016, for review). Active galactic nuclei (AGNs) activity can impact the host galaxy and the tenuous environment by ionizing or photo-dissociating the gas, heating the halo gas and reducing the rate of cold accretion onto the galaxy, and/or driving fast outflows that eject gas to large galactocentric distances and, thus in powerful AGNs, temporarily or permanently

suppressing star formation (SF) by removing the gas supply from massive galaxies (see Somerville & Davé 2015, for a review).

Global changes in the metallicity of galaxies are driven by stellar nucleosynthesis, and thus, it is fundamental to connect it with the star formation history (SFH) in galaxies. AGNs are crucial components of theoretical models of galaxy formation and evolution used in regulating the SF in galaxies. The constant gas ejection or heating and, as a result, SF suppression is expected in massive galaxies ( $\sim 10^{10} M_\odot$ ) because of AGN nuclear emission. Although this mechanism is an important component of numerical simulations of galaxy formation, observational studies have not yet conclusively supported it. The negative AGN feedback from observational study is required for many findings to be reproduced by theoretical models, such as the substantial suppression of SF in the most massive galaxies (e.g. Springel, Di Matteo & Hernquist 2005; Hopkins & Elvis 2010;

\* E-mail: [armah@ufrgs.br](mailto:armah@ufrgs.br) (MA); [riffel@ufrgs.br](mailto:riffel@ufrgs.br) (RR)

Brownson et al. 2020; Smith et al. 2020). AGN-driven winds, shock compression or gas accretion may also cause SF in the host galaxy, a phenomenon known as positive feedback (e.g. Elbaz et al. 2009; Silk 2013; Maiolino et al. 2017; Salomé et al. 2017; Gallagher et al. 2019; Kawamuro et al. 2021; Koss et al. 2021). However, some studies, particularly for moderate-luminosity AGNs, claim that star formation is independent of AGN activity (e.g. Stanley et al. 2015; Suh et al. 2019). From the foregoing, it is safe to posit that galaxy-scale warm-ionized and cold molecular outflows, which are powered by actively accreting SMBHs and traced by rest-frame optical (Heckman et al. 1981) and carbon monoxide (CO; Cicone et al. 2014) emission lines respectively, can be associated with both the suppression and triggering of star formation. However, a thorough understanding of the interactions between AGN accretion and star formation processes of the host galaxy is required to fully understand galaxy formation and evolution.

The elemental abundance and metallicity ( $Z$ )<sup>1</sup> estimations in the gas phase of AGNs are essential in the study of the chemical evolution of galaxies. The gas phase metallicity can be derived in both star-forming regions (SFs, i.e. H II regions and star-forming galaxies) and AGNs through direct estimation of the electron temperature, usually known as  $T_e$ -method<sup>2</sup> and strong-line methods.<sup>3</sup> It is worthwhile to note that SFs are ionized by massive stars (e.g. O- or early B-type stars), while AGNs have harder radiation fields as their ionization sources. Therefore, applying SFs metallicity formalism to AGNs will yield systematically biased metallicities (e.g. Dors et al. 2020b). There is consensus that the  $T_e$ -method is the most reliable approach to estimate metallicity and elemental abundances in SFs (Pilyugin 2003; Toribio San Cipriano et al. 2017). Recently, Dors et al. (2020b) proposed a new methodology of the  $T_e$ -method for AGNs which produces reliable O/H abundances lower ( $\lesssim 0.2$  dex) than those derived from detailed photoionization models. For the first time, Armah et al. (2021), Monteiro & Dors (2021), and Dors et al. (2022), motivated by this new methodology derived the neon, argon and helium abundances, respectively, in 164 local Seyfert 2 nuclei ( $z \lesssim 0.25$ ). The  $T_e$ -method requires measurements of auroral lines (e.g. [O III] $\lambda 4363$ , [N II] $\lambda 5755$ , [S III] $\lambda 6312$ ) which are weak ( $\sim 100$  times weaker than H  $\beta$ ) and detected only in objects with high ionization and/or low metallicity (e.g. van Zee et al. 1998; Díaz et al. 2007; Dors et al. 2008). Thus, it is impossible to derive a direct measurement of abundance from the emission lines if the critical emission-line diagnostics for electron temperature and, to some extent, electron density are unavailable. To circumvent this problem, Pagel et al. (1979), following the original idea by Jensen, Strom & Strom (1976), proposed a calibration between strong-emission lines, in the case of [O III] $(\lambda 4959 + \lambda 5007)/H \beta$ , and the O/H abundance. Thereafter this pioneering work, several authors have proposed calibrations for SFs (e.g. Marino et al. 2013; Pilyugin & Grebel 2016; Curti et al. 2017; Jiang et al. 2019, and references therein) and for AGNs (e.g. Storch-

Bergmann et al. 1998; Dors et al. 2014, 2019; Castro et al. 2017; Carvalho et al. 2020; Dors 2021, among others).

Therefore, by comparing AGN luminosity ( $L_{\text{AGN}}$ ) and the metallicity, it is possible to study the origin and evolution of SMBHs and their host galaxies (e.g. Wang et al. 2010). Previous studies have shown a distinct relation between the metallicity from the narrow-line region ( $Z_{\text{NLR}}$ ) and the  $L_{\text{AGN}}$  (e.g. Netzer et al. 2004; Nagao, Maiolino & Marconi 2006; Matsuoka et al. 2009). The ionized gas mass of the NLR is  $M_{\text{NLR}} \sim 10^{5-7} M_{\odot}$ , which is far greater than that of the broad-line region (BLR) i.e.  $M_{\text{BLR}} \sim 10^{2-4} M_{\odot}$  (e.g. Osterbrock 1989; Baldwin et al. 2003a), suggesting that the  $L_{\text{AGN}}-Z_{\text{NLR}}$  relation is an indication that AGN gas metallicity traces the gas enrichment in its host galaxy. Since the BLR has a very small radius (e.g.  $R_{\text{BLR}} < 1$  pc; Kaspi et al. 2000; Bennert et al. 2006b; Sugauma et al. 2006) because of its proximity to the central source as compared to the NLR (e.g.  $R_{\text{NLR}} \sim 10^{1-4}$  pc; Bennert et al. 2006a) in galactic nuclei, the  $L_{\text{AGN}}-Z_{\text{NLR}}$  relation will be a better tracer of the evolution of the host galaxy than the metallicity from the BLR ( $L_{\text{AGN}}-Z_{\text{BLR}}$  relation). Also,  $Z_{\text{NLR}}$  may be uniquely promising and better suited as a proxy for the properties of the host galaxy since the spatial extent of the NLR region is larger than the BLR in low- and high- $z$  as well as high  $L_{\text{AGN}}$ , as observed by the strong correlation between the size of the NLR and the  $L_{\text{AGN}}$  of the optical [O III] $\lambda 5007$  emission line (e.g. Dempsey & Zakamska 2018; Sun et al. 2018; Chen et al. 2019). Moreover,  $Z_{\text{NLR}}$  values have been found to be either solar or near the solar metallicity ( $Z_{\odot}$ ) i.e.  $0.2 \lesssim (Z_{\text{NLR}}/Z_{\odot}) \lesssim 1$  (e.g. Nagao et al. 2006; Dors et al. 2019), hence  $Z_{\text{BLR}}$  estimates at all redshifts are higher by a factor of 2–15 times  $Z_{\text{NLR}}$  (e.g. Hamann & Ferland 1993; Baldwin et al. 2003b; Bentz, Hall & Osmer 2004; Tang et al. 2019; Garnica et al. 2022), which indicates that the  $Z_{\text{BLR}}$  is not representative of the metallicity of the host galaxy, which is better traced by the  $Z_{\text{NLR}}$ . Although the BLRs are located in objects with high mass, where high metallicity values are expected (e.g. Xu et al. 2018), the higher  $Z_{\text{BLR}}$  values which are indirectly inferred from metallicity-sensitive broad emission-line flux ratios seem to be unreal (e.g. Temple et al. 2021, consideration for changes in the physical conditions of the emitting gas before metallicity estimation) as compared to direct estimates of the  $Z_{\text{NLR}}$  values. However, most of the  $Z_{\text{NLR}}$  studies have been based on small samples of objects and/or with no  $L_{\text{AGN}}-Z_{\text{NLR}}$  relation studies (see Dors et al. 2020a, for example).

The stellar mass–metallicity relation (MZR; e.g. Tremonti et al. 2004; Boardman et al. 2022) indicates that the metallicities of galaxies increase with increasing stellar masses, while the fundamental metallicity relation (FMR; e.g. Lilly et al. 2013; Pistis et al. 2022) suggests that, for a given stellar mass, galaxies with higher star formation rates (SFRs) tend to have lower metallicities. For the first time, Matsuoka et al. (2018) found a correlation between  $Z_{\text{NLR}}$  and the host galaxy mass ( $M_{\star}-Z_{\text{NLR}}$  relation) for objects at  $z \sim 3$ . A comparison between observed ultraviolet emission-line flux ratios and photoionization model predictions by these authors showed that  $Z_{\text{NLR}}$  increases by  $\sim 0.7$  dex as  $\log(M_{\star}/M_{\odot})$  increases from  $\sim 10$  to  $\sim 12$ . This relation was also confirmed by Dors et al. (2019) for type 2 AGNs in a wider redshift range ( $1.6 < z < 3.8$ ) following a similar methodology by Matsuoka et al. (2018). Both studies indicate that AGNs and their host galaxies have similar metal enrichment and the  $M_{\star}-Z_{\text{NLR}}$  relation seems to complement similar estimates from star-forming galaxies (see Maiolino et al. 2008) for  $z \sim 3.5$  towards higher masses.

On the other hand, for the local Universe, a different scenario is found. For instance, Thomas et al. (2019) used the Bayesian code (NEBULABAYES) which is based on photoionization model

<sup>1</sup>The gas-phase metallicity is usually calculated as the oxygen abundance relative to hydrogen, and defined in units of  $[12 + \log(\text{O}/\text{H})]$ . Oxygen is used to define the overall gas-phase metallicity because it presents prominent temperature-sensitive collisionally excited lines (e.g.  $\text{O}^+$ : [O II] $\lambda 3727$  and  $\text{O}^{2+}$ : [O III] $\lambda 4363$ , [O III] $\lambda 5007$ ) in the optical spectrum of gaseous nebulae. For brevity, oxygen abundance and metallicity are used interchangeably in this work.

<sup>2</sup>For a review of the  $T_e$ -method for SFs see Peimbert, Peimbert & Delgado-Inglada (2017), Pérez-Montero (2017), and AGNs see Dors et al. (2020b).

<sup>3</sup>For a review of strong-line methods for SFs and AGNs see Lopez-Sanchez & Esteban (2010) and Dors et al. (2020a), respectively.

fitting of several optical emission lines and found that the  $Z_{\text{NLR}}$  increases by  $\Delta(\text{O}/\text{H}) \sim 0.1$  dex as a function of the  $M_*$  over the range  $10.1 \lesssim \log(M_*/M_\odot) \lesssim 11.3$ . However, this  $Z_{\text{NLR}}$  increase is lower than the uncertainty produced by the strong-line methods (e.g. Storchi-Bergmann et al. 1998; Denicoló, Terlevich & Terlevich 2002) or by the  $T_e$ -method (e.g. Berg et al. 2020; Dors et al. 2022). Moreover, Dors et al. (2020a) applied all the methods available in the literature for deriving  $Z_{\text{NLR}}$  using spectroscopic data from SDSS-DR7 (York et al. 2000; Abazajian et al. 2009) but could not confirm the  $M_*$ - $Z_{\text{NLR}}$  relation for local objects ( $z \lesssim 0.4$ ).

The aforementioned MZR studies suggest some discrepancies between the results from various studies and raise the question of whether there are differences in the  $L_{\text{AGN}}-Z_{\text{NLR}}$  and MZR relations between the global parameters of low or/and high redshift(s) in AGNs, or if they are driven by small samples or due to the effects of the various selection criteria and methods have on the  $Z$  of galaxies. In view of this, we apply the strong-line methods to analyse the  $L_X-Z_{\text{NLR}}$  relation using optical and X-ray data from a large sample of X-ray selected AGNs in this current study. In principle, the X-ray luminosity can yield more reliable results than the stellar mass because X-ray surveys are practically efficient for selecting AGNs since X-ray emissions are generated from the nuclear components with relatively clean signals which are less affected by obscuration and contamination from non-nuclear emissions. Hitherto, almost all the  $L_{\text{AGN}}-Z_{\text{NLR}}$  and  $L_{\text{AGN}}-Z_{\text{BLR}}$  relations in the literature have been obtained based on either optical or UV selection criteria. However, the hard ( $\gtrsim 10$  keV) X-ray luminosity ( $L_X$ ) of the *Swift*-BAT AGN Spectroscopic Survey (BASS; see Ricci et al. 2017a, for details) which have been relied on in this work, measures direct emission from the AGN which is unaffected by dust or contamination from SF, and is much less sensitive to obscuration in the line-of-sight as compared to soft X-ray or optical wavelengths, allowing a selection based on only the central engine properties. Compact, nuclear, and luminous X-ray emission is certainly a sign of an AGN due to the compact and dense plasma required to produce X-ray emission since at low- $z$  an X-ray luminosity e.g.  $L_X > 10^{42}$  erg s $^{-1}$  cannot be produced by anything else other than an accreting SMBH. Therefore, we compare the metallicity derived from optical emission lines of these hard X-ray selected AGNs with their X-ray properties to better understand the AGN  $L_X-Z$  relation. This paper is organized as follows. We describe the observational data in Section 2. Details to the calculations of the total oxygen abundances via the strong-line methods have been outlined in Section 3. The results and discussions are presented in Section 4. Finally, we summarize our findings in Section 5. Throughout this paper, we adopt a spatially flat  $\Lambda$ CDM cosmology with the parameters:  $\Omega_M = 0.3$ ,  $\Omega_\Lambda = 0.7$ , and  $H_0 = 70$  km s $^{-1}$  Mpc $^{-1}$ .

## 2 OBSERVATIONAL DATA AND SAMPLE DESCRIPTION

To calculate the oxygen abundances for the narrow line region of a sample of Seyfert nuclei, optical spectroscopic data taken from the literature are considered. Therefore, we selected AGN emission line intensities from the BASS DR2 presented by (Oh et al. 2022) for the O/H estimations. It is worth mentioning that these authors have taken special care to remove the broad components from the allowed emission lines as well as removing possible outflow asymmetries effects from the emission line fluxes (for details see Oh et al. 2022). In order to compare these abundances with AGN properties (e.g.  $L_X$ , Eddington ratios) we cross-matched this sample with the BASS DR2, which provides X-ray observed and intrinsic

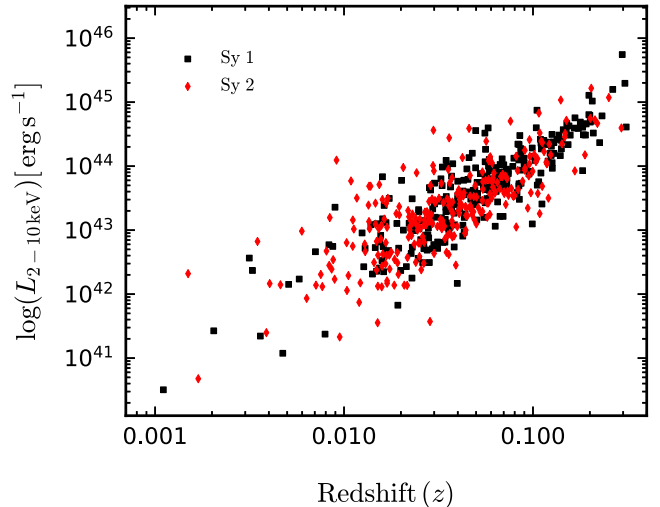


**Figure 1.** Redshift distribution of the rest-frame hard X-ray luminosity based on the 2–10 keV emissions of the BAT AGNs. Points with different colours represent the observed 2–10 keV luminosities for Sy 1 and Sy 2 of the sources in our sample with spectroscopic redshifts, as indicated.

luminosities (Ricci et al. 2017a), resulting in 743 common sources, more details are given below (see Section 2.1). The luminosity values for the AGN sample are those measured in the two X-ray bands, 2–10 keV and 14–195 keV, and the metallicity estimated are calculated through optical emission lines. Fig. 1 shows a plot of the selected X-ray luminosities in the *Swift*-BAT AGN sample together with their corresponding redshifts. Points with different colours represent the observed 2–10 keV luminosities for all the sources in our sample with spectroscopic redshifts.

### 2.1 The 70-month *Swift*-BAT Catalog and the emission line fluxes

The Burst Alert Telescope (BAT) instrument onboard the *Swift* satellite (Gehrels et al. 2004), which is undertaking an all-sky survey in the ultra-hard X-ray band (14–195 keV), has identified 1210 objects (Baumgartner et al. 2013), of which 858 are classified as AGNs (Koss et al. 2022a) based on their cross-correlations with objects in the medium and soft energy X-ray bands.

The optical emission line fluxes (3200–10 000 Å) of 743 sources presented by Oh et al. (2022) in the BASS DR2 were considered in this work. A complete summary of the instrument setups and observing parameters have been provided by Koss et al. (2022a). The BASS DR2 used targeted observations with the Palomar Double Spectrograph (DBSP), which is attached to the Hale 200-inch telescope (36.4 per cent, 271/743), the X-Shooter spectrograph mounted on the European Southern Observatory’s *Very Large Telescope* (ESO-VLT; 22.7 per cent, 169/743; Vernet et al. 2011), the Boller & Chivens (B & C) spectrograph mounted on the 2.5-m *Irénée du Pont* telescope at the Las Campanas Observatory (5.5 per cent, 41/743), observations from the Goodman spectrograph (4.3 per cent, 32/743; Clemens; Crain & Anderson 2004) on the *Southern Astrophysical Research* (SOAR) telescope, and the low-resolution imaging spectrometer (LRIS; 0.7 per cent, 5/743; Oke et al. 1995) on the *Keck* telescope. Spectra from publicly available surveys, such as SDSS Data Release 15 (15.9 per cent, 118/743; Aguado et al. 2019), and 71 AGN spectra (see Koss et al. 2017) that were not in the DR2 were also used.

Due to its selection from the hard X-ray band (14–195 keV), the BASS sample is almost insensitive to obscuration up to Compton-thick levels ( $N_{\text{H}} > 10^{24} \text{ cm}^{-2}$ ; Ricci et al. 2015; Koss et al. 2016). Koss et al. (2017, 2022a) and Oh et al. (2022) have given a detailed overview of the optical spectroscopic data. Additionally, extended multi-wavelength campaigns from near-infrared (NIR) to soft X-ray wavelengths have made it possible to further characterize the BASS sample, for the scaling between global galaxy properties such as the correlations between X-ray and optical obscuration, NIR lines, X-ray photon index, absorption, and coronal properties, AGN mass outflow rates and bolometric luminosity (e.g. Berney et al. 2015; Lamperti et al. 2017; Oh et al. 2017; Ricci et al. 2017b, 2018; Trakhtenbrot et al. 2017; Liu et al. 2020; Rojas et al. 2020; Koss et al. 2021; Ananna et al. 2022; Kakkad et al. 2022; Ricci et al. 2022, among others).

## 2.2 Our final sample

We selected Seyfert galaxies from the second catalogue and data release of the BASS made available by Oh et al. (2022). For a better comparison with previous works with regards to the oxygen abundance, we consider only sources classified as Seyferts based on diagnostic diagrams (see Section 2.3 below) as suggested by Baldwin, Phillips & Terlevich (1981). We consider the diagrams  $[\text{O III}]\lambda 5007/\text{H}\beta$  versus  $[\text{N II}]\lambda 6583/\text{H}\alpha$ ,  $[\text{S II}]\lambda\lambda 6717, 6731/\text{H}\alpha$ , and  $[\text{O I}]\lambda 6300/\text{H}\alpha$  that require the theoretical demarcation lines used by Kewley et al. (2001, 2006) proposed to separate AGNs, transition, and star-forming regions, and the empirical line proposed by Schawinski et al. (2007) to separate Seyferts from LI(N)ERs (also see Cid Fernandes et al. 2010).

Considering the selected Seyferts sample, we applied criteria for the optical data which consists of emission lines observed in the wavelength range of  $3500 < \lambda(\text{\AA}) < 7000$  as well as the  $L_{\text{X}}$ . These criteria are underscored below:

(i) The objects must have the narrow optical  $\text{H}\beta$   $\lambda 4861$ ,  $[\text{O III}]\lambda 5007$ ,  $\text{H}\alpha$   $\lambda 6563$ ,  $[\text{N II}]\lambda 6584$ , and  $[\text{S II}]\lambda\lambda 6716, 6731$  emission-line fluxes measured, which gives a total sample consisting of 561 objects. We started with 743 sources, excluded 138 because they were not within Seyfert region (including 56 LI(N)ERs), 44 AGNs with high obscuration and non-detection of  $\text{H}\beta$  were also discarded. We define Sy 1 as the sources with Sy 1–1.5 classification as defined by Oh et al. (2022) based on the strength of  $[\text{O III}]$  to  $\text{H}\beta$  and Sy 2 as those with Sy 1.8–2 classification.<sup>4</sup> Therefore, the 561 objects comprise of 287 Sy 1s and 274 Sy 2s where the emission lines were detected at  $\lesssim 3\sigma$  significance level for each target. This selection criterion permits to estimate the NLRs metallicities based on several strong-line methods (see Dors et al. 2020a, for a review of the methods).

(ii) Finally, we selected objects with estimated Eddington ratios,  $\lambda_{\text{Edd}} = L_{\text{bol}}^{\text{int}}/L_{\text{Edd}}$  to analyse the  $L_{\text{X}}-\lambda_{\text{Edd}}$  relation. We obtained a subsample for 282 Sy 1s and 264 Sy 2s from Koss et al. (2022a) with Eddington ratio estimates based on the intrinsic X-ray emission and black hole masses using velocity dispersions (Koss et al. 2022b) and broad Balmer lines (Mejía-Restrepo et al. 2016). Thus, we note that the analysis involving these quantities are with smaller samples than those with only  $L_{\text{X}}$ .

<sup>4</sup>This choice was made because objects classified as Sy 1.8 shows very weak broad  $\text{H}\beta$  and  $\text{H}\alpha$  in its optical spectrum while in Sy 1.9 only the weak broad component is detected at  $\text{H}\alpha$  (e.g. Osterbrock 1981), thus their overall spectrum is more close to a type 2 source than to a true type 1.

We chose only the strong-line methods to determine the abundances because when the presence of the  $[\text{O III}]\lambda 4363$  line is considered in the selection criteria for the sources, the sample will considerably be reduced to 218/561 sources. Moreover, considering the  $T_{\text{e}}$ -method will lead to selection effect, specifically the high degree of uncertainties in the measurements of the strengths of the weak temperature-sensitive auroral oxygen line  $[\text{O III}]\lambda 4363$  given that  $[\text{O III}]\lambda 4363$  emission line should be at rest with respect to the  $T_{\text{e}}$ -method associated rest-optical nebular emission lines, which could potentially introduce similar margin of high degree of uncertainties in the oxygen abundances derived using the  $T_{\text{e}}$ -method.

## 2.3 Diagnostic diagrams

Although the objects considered in the present work have been classified as AGNs by the original authors, for consistency with our previous works we produced an additional test for a homogeneous sample selection based on the standard Baldwin–Phillips–Terlevich (BPT; Baldwin et al. 1981; Veilleux & Osterbrock 1987) diagrams. Here we adopted the theoretical criterion which relied on photoionization model results, proposed by Kewley et al. (2001, 2006), where emission line objects with

$$\log([\text{O III}]\lambda 5007/\text{H}\beta) > \frac{0.61}{[\log([\text{N II}]\lambda 6584/\text{H}\alpha) - 0.47]} + 1.19, \quad (1)$$

$$\log([\text{O III}]\lambda 5007/\text{H}\beta) > \frac{0.72}{[\log([\text{S II}]\lambda 6725/\text{H}\alpha) - 0.32]} + 1.30, \quad (2)$$

and

$$\log([\text{O III}]\lambda 5007/\text{H}\beta) > \frac{0.73}{[\log([\text{O I}]\lambda 6300/\text{H}\alpha) + 0.59]} + 1.33 \quad (3)$$

are classified as AGNs. The  $[\text{S II}]\lambda 6725$  line represents the sum of the  $[\text{S II}]\lambda 6717, \lambda 6731$  doublet. Fig. 2 shows the diagnostic diagrams using the emission-line ratios of  $\log([\text{O III}]\lambda 5007/\text{H}\beta)$  versus  $\log([\text{N II}]\lambda 6584/\text{H}\alpha)$ ,  $\log([\text{S II}]\lambda 6725/\text{H}\alpha)$ , and  $\log([\text{O I}]\lambda 6300/\text{H}\alpha)$  for our sample of galaxies. The dashed line shown in this figure represents the criterion proposed by Schawinski et al. (2007) to separate AGN-like and low ionisation (nuclear) emission line regions [LI(N)ERs] objects, given by

$$\log([\text{O III}]\lambda 5007/\text{H}\beta) > 0.45 + \log([\text{N II}]\lambda 6584/\text{H}\alpha) \times 1.05. \quad (4)$$

We notice that the objects cover a large range of ionization degree and metallicity since a wide range of  $[\text{O III}]/\text{H}\beta$  and  $[\text{N II}]/\text{H}\alpha$  are observed (e.g. Feltre, Charlot & Gutkin 2016; Castro et al. 2017; Ji et al. 2020; Agostino et al. 2021).

## 2.4 Reddening correction

Seyfert galaxies can be strongly affected by internal reddening (see Schnorr-Müller et al. 2016; Lu et al. 2019, for example). However, the internal extinction can be derived from the ratio of the strongest recombination lines of hydrogen in the optical spectrum i.e.  $\text{H}\alpha/\text{H}\beta$ . For a pure recombination and a temperature of  $10^4 \text{ K}$ , this ratio is expected to have the value  $\text{H}\alpha/\text{H}\beta = 2.86$  (Case B recombination; Osterbrock 1989). An observed ratio higher than this value can thus be attributed to reddening from dust. The corresponding colour

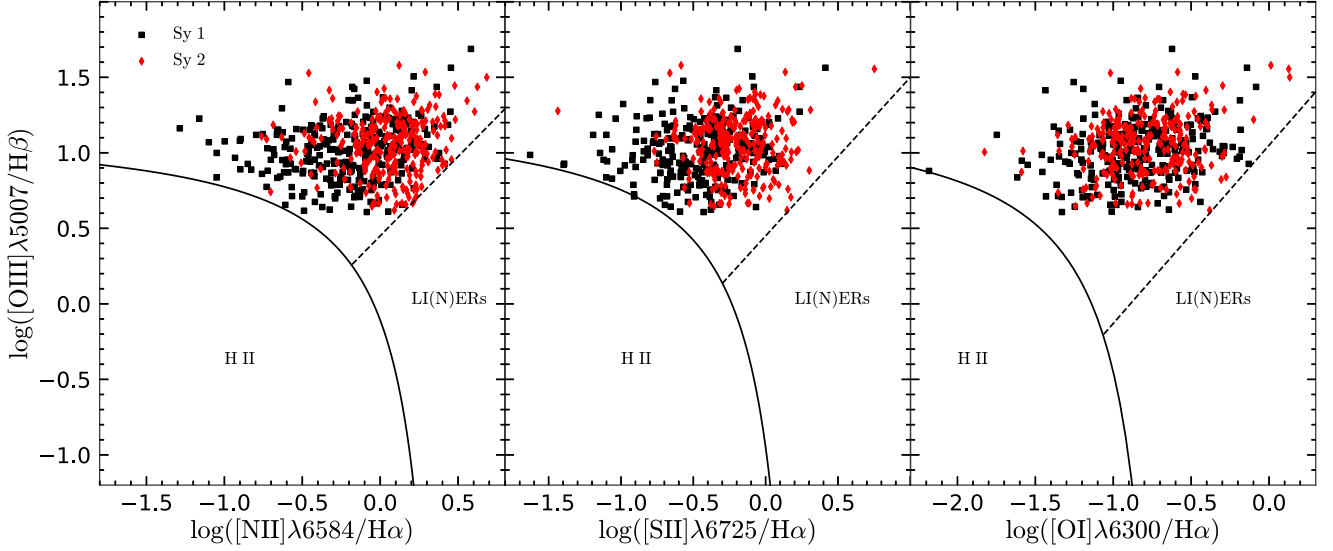


**Figure 2.** Diagnostic diagrams for emission-line ratios of  $\log([\text{O III}]\lambda 5007/\text{H}\beta)$  versus  $\log([\text{N II}]\lambda 6584/\text{H}\alpha)$ ,  $\log([\text{S II}]\lambda 6725/\text{H}\alpha)$ , and  $\log([\text{O I}]\lambda 6300/\text{H}\alpha)$ .  $[\text{S II}]\lambda 6725$  represents the sum of the lines  $[\text{S II}]\lambda 6717$  and  $[\text{S II}]\lambda 6731$ . Points represent objects of our sample (see Section 2). Solid lines, by Kewley et al. (2001) and represented by equations (1), (2), and (3), separate objects ionized by massive stars from those ionized by AGN-like objects, as indicated. The dashed lines represent the criterion proposed by Schawinski et al. (2007) to separate AGN-like and low ionisation (nuclear) emission line regions [LI(N)ERs] objects, given by equation (4). Red and black points represent the emission lines from the NLRs of Seyferts 1 and 2 respectively, as indicated.

excess from this ratio is expressed as

$$\begin{aligned} E(B - V) &= \frac{E(\text{H}\beta - \text{H}\alpha)}{f_\lambda(\text{H}\beta) - f_\lambda(\text{H}\alpha)} \\ &= \frac{2.5}{R_\lambda [f_\lambda(\text{H}\beta) - f_\lambda(\text{H}\alpha)]} \left[ \frac{(F_{\text{H}\alpha}/F_{\text{H}\beta})^{\text{obs}}}{(F_{\text{H}\alpha}/F_{\text{H}\beta})^{\text{int}}} \right], \end{aligned} \quad (5)$$

where  $R_\lambda [f_\lambda(\text{H}\beta) - f_\lambda(\text{H}\alpha)]$  are the Galactic extinction coefficients,  $f_\lambda(\text{H}\beta)$  and  $f_\lambda(\text{H}\alpha)$  are the reddening curve values at the  $\text{H}\beta$  and  $\text{H}\alpha$  wavelengths, respectively. The logarithmic extinction coefficient,  $c(\text{H}\beta)$ , is the reddening constant simply defined as

$$c(\text{H}\beta) = \frac{R_\lambda [f_\lambda(\text{H}\beta)]}{2.5} E(B - V) \quad (6)$$

The final logarithmic extinction coefficient can be thus calculated from the following relation as

$$c(\text{H}\beta) = -\frac{1}{f(\lambda) - f(\text{H}\beta)} \cdot \left[ \log \left( \frac{F(\lambda)}{F(\text{H}\beta)} \right) - \log \left( \frac{I(\lambda)}{I(\text{H}\beta)} \right) \right]. \quad (7)$$

An extinction correction can then be applied to all observed emission line fluxes, normalized to the  $\text{H}\beta$  flux using

$$\frac{I(\lambda)}{I(\text{H}\beta)} = \frac{F(\lambda)}{F(\text{H}\beta)} \times 10^{-c(\text{H}\beta)[f(\lambda) - f(\text{H}\beta)]}, \quad (8)$$

where  $I(\lambda)$  is the intensity (reddening corrected) of the emission line at a given wavelength  $\lambda$ ,  $F(\lambda)$  is the observed flux of the emission line,  $f(\lambda)$  is the adopted reddening curve normalized to  $\text{H}\beta$  and  $c(\text{H}\beta)$  is the interstellar extinction coefficient. The  $[f(\lambda) - f(\text{H}\beta)]$  values were compiled from table 7.1 by Osterbrock (1989). In order to provide supplementary interpolation data for further important nebular emission lines between different specific wavelength-dependent extinction factor  $f(\lambda)$  values since not all lines

were listed, we have derived the following reddening function,<sup>5</sup>

$$f(\lambda) = 2.967\lambda^2 - 5.454\lambda + 1.953, \quad (9)$$

with  $\lambda$  in units of micrometers within the range  $0.35 \lesssim \lambda(\mu\text{m}) \lesssim 0.70$ .

Halpern (1982) and Halpern & Steiner (1983) used photoionization models and found that  $I(\text{H}\alpha/\text{H}\beta)$  is  $\sim 3.10$  in AGNs with high and low ionization degree in comparison to the canonical Case B recombination value of 2.86. Therefore,  $I(\text{H}\alpha/\text{H}\beta) = 2.86$  and 3.10 intrinsic ratios are usually considered to be estimations for galaxies dominated by star formation and for galaxies dominated by AGNs, respectively (Gaskell 1982, 1984; Ferland & Netzer 1983; Gaskell & Ferland 1984; Veilleux & Osterbrock 1987; Wysota & Gaskell 1988). Particularly, in AGNs, there is a large transition zone, or partly ionized region, in which  $\text{H}^0$  coexists with  $\text{H}^+$  and free electrons (see Dors et al. 2022, and references therein). In this zone, collisional excitation is also important in addition to recombination (Ferland & Netzer 1983; Halpern & Steiner 1983). The main effect of collisional excitation is to enhance the intensity of  $\text{H}\alpha$ . The higher Balmer lines are less affected because of their large re-excitation energies and smaller excitation cross-sections. With this in mind, we have corrected the emission-line fluxes for extinction using the Balmer decrement and the Cardelli, Clayton & Mathis (1989) reddening curve for the internal and Galactic reddening, respectively. We assumed an  $R_V = A_V/E(B - V) = 3.1$  and an intrinsic  $\text{H}\alpha/\text{H}\beta = 3.1$ .

Since some measurements for the emission lines do not have their uncertainties listed ( $\text{H}\beta$ : 29/561,  $\text{H}\alpha$ : 1/561,  $[\text{O III}]\lambda 4959$ : 25/561,  $[\text{O III}]\lambda 5007$ : 5/561,  $[\text{N II}]\lambda 6548$ : 63/561,  $[\text{N II}]\lambda 6584$ : 6/561, and  $[\text{S II}]\lambda\lambda 6716, 6731$ : 31/561 each), thus, we adopted a typical error

<sup>5</sup>The wavelength dependence in the optical domain,  $f(\lambda)$  is the reddening value for the line derived from the curve given by  $[f(\lambda) - f(\text{H}\beta)]$ , such that  $f(\infty) = -1$  and  $f(\text{H}\beta) = 0$  yields to the curve, considering the rest-frame wavelengths for permitted and forbidden lines from Moore (1945) and Bowen (1960), respectively.

of 10 per cent (see, for instance, Kraemer et al. 1994; Hägele et al. 2008). These errors were propagated through the estimations of the uncertainties in the derived values of the metallicity (in order of 0.1 dex). It worth to note that, for a lower redshift limit of  $z < 0.04$ , extraction aperture of 1.5–2 arcsec (Koss et al. 2022a) in radius and the aperture covering fraction of  $\sim 20$  per cent are sufficient for avoiding aperture effects on our metallicity estimates (see Kewley, Jansen & Geller 2005; Kewley & Ellison 2008). Additionally, these authors posited that the derived metallicity can vary by  $\sim 0.14$  dex from the value determined when the total galaxy emission is taken into account for apertures that capture less than 20 per cent of the total galaxy emission. However, only the nuclear region abundances are considered in our study, so the aperture effect on our metallicity estimates is insignificant.

### 3 METHODOLOGY

The main goal of this work is to derive the oxygen abundance relative to hydrogen (O/H) from the NLRs of a sample of Seyfert nuclei in order to analyse the  $L_X$ – $Z_{\text{NLR}}$  relation. In view of that, we adopted the strong-line methods for optical emission lines to be applied in the studies of the NLR of Seyfert nuclei. In the following sections we describe to somewhat details of the aforementioned methods and the oxygen abundance computed from the data under consideration in this work.

#### 3.1 AGN calibrations

In recent optical surveys such as the Sloan Digital Sky Survey (SDSS; York et al. 2000), the  $[\text{O II}]\lambda 3727$  line is measured in very few objects. Moreover,  $[\text{O II}]\lambda 3727$  line is more in the bluer part of the spectrum and it is more effectively scattered or affected by interstellar reddening. Furthermore, more than one-half of the current strong-line calibrations derived for AGNs consider the  $[\text{O II}]\lambda 3727$  line as data selection criterion (e.g. Storchi-Bergmann, Calzetti & Kinney 1994; Castro et al. 2017; Dors 2021). Therefore, we note that when the presence of the  $[\text{O II}]\lambda 3727$  line is considered in the selection criteria of objects, the sample is considerably reduced. Hitherto, the only AGN calibrations which solely rely on  $[\text{N II}]\lambda \lambda 6548, 6584/H\alpha$  and/or  $[\text{O III}]\lambda \lambda 4959, 5007/H\beta$  are the two calibrations proposed by Storchi-Bergmann et al. (1998) and Carvalho et al. (2020). We provide descriptions of these calibrations in the following sections.

##### 3.1.1 Storchi-Bergmann et al. (1998) calibration

Storchi-Bergmann et al. (1998) used grid of photoionization models by assuming a typical AGN continuum, which were built with the CLOUDY code (Ferland et al. 2017) and, for the first time proposed two AGN theoretical calibrations between the NLRs emission line ratios  $[\text{N II}]\lambda \lambda 6548, 6584/H\alpha$ ,  $[\text{O II}]\lambda 3727/[\text{O III}]\lambda \lambda 4959, 5007$  as well as  $[\text{O III}]\lambda \lambda 4959, 5007/H\beta$  and the metallicity (traced by the oxygen abundance). The models were constructed assuming a gas density value of  $300 \text{ cm}^{-3}$ , and the calibrations were fitted within  $\sim 0.05$  dex of the models. These calibrations are valid for the range of  $8.4 \lesssim [12 + \log(\text{O}/\text{H})] \lesssim 9.4$  and the oxygen abundances obtained from these calibrations differ systematically by only  $\sim 0.1$  dex (Storchi-Bergmann et al. 1998; Dors et al. 2020a).

In this work we used only one calibration proposed by Storchi-Bergmann et al. (1998, hereafter **SB98f1**) because using the  $[\text{O II}]\lambda 3727$  line as a selection criterion will reduce the number of

sources to 396/561. The **SB98f1** calibration is defined by

$$12 + (\text{O}/\text{H}) = 8.34 + (0.212x) - (0.012x^2) - (0.002y) \\ + (0.007xy) - (0.002x^2y) + (6.52 \times 10^{-4}y^2) \\ + (2.27 \times 10^{-4}xy^2) + (8.87 \times 10^{-5}x^2y^2), \quad (10)$$

where  $x = [\text{N II}]\lambda \lambda 6548, 6584/H\alpha$  and  $y = [\text{O III}]\lambda \lambda 4959, 5007/H\beta$ .

It is important to apply the correction proposed by these authors to equation (10) in order to account for the deviations from the assumed gas density therefore the final calibration is given by

$$\log(\text{O}/\text{H})_{\text{SB98f1}} = [\log(\text{O}/\text{H})] - \left[ 0.1 \times \log \frac{N_e(\text{cm}^{-3})}{300(\text{cm}^{-3})} \right], \quad (11)$$

where  $N_e$  is the electron density and equation (11) is valid for  $10^2 \lesssim N_e(\text{cm}^{-3}) \lesssim 10^4$ .

##### 3.1.2 Electron density

The electron density ( $N_e$ ), for each object, was calculated from the  $[\text{S II}]\lambda \lambda 6717, 6731$  doublet flux ratio, using the 1.1.16 version of PYNEB code (Luridiana, Morisset & Shaw 2015) and assuming a constant electron temperature  $T_e = 10^4$  K, typical for photoionized gas in the NLRs. The PYNEB code allows an interactive procedure where  $N_e$  is computed from the required forbidden lines depending on specific value of  $T_e$ . Moreover, it is worth mentioning that  $[\text{S II}]\lambda \lambda 6717, 6731$  can only be applied to  $0.45 \lesssim R_{[\text{S II}]} \lesssim 1.45$  (where  $R_{[\text{S II}]} = F_{\lambda 6717}/F_{\lambda 6731}$ , see Osterbrock & Ferland 2006; Sanders et al. 2016), which translates into electron density values in the range of  $5000 \gtrsim N_e(\text{cm}^{-3}) \gtrsim 50$ , respectively. Therefore, for the objects with emission line ratios outside these theoretical constraints, we assumed the electron density to be  $N_e = 2000 \text{ cm}^{-3}$  if  $R_{[\text{S II}]} \lesssim 0.45$ , in order to avoid collisional de-excitation<sup>6</sup> effect and  $N_e = 100 \text{ cm}^{-3}$  if  $R_{[\text{S II}]} \gtrsim 1.45$ , which is the minimum electron density value for the calibration by **SB98f1**. From the 561 objects considered for the strong-line method calibrations,<sup>7</sup> there are 5 with  $R_{[\text{S II}]} \lesssim 0.45$  and 62 with  $R_{[\text{S II}]} \gtrsim 1.45$  i.e.  $\sim 12$  per cent of the total sample. While some of the  $R_{[\text{S II}]}$  values are extreme and beyond the low-density regime other emission lines from the sources are not aberrant.

In order to verify if there is a correlation between the electron density and the intensity of the strong emission line ratios involved in the metallicity calculations, in Fig. 3, we plotted the logarithm of  $[\text{O III}]\lambda 5007/H\beta$  (top panel),  $[\text{N II}]\lambda 6584/H\alpha$  (middle panel), and  $[\text{S II}]\lambda 6725/H\alpha$  (bottom panel) versus  $R_{[\text{S II}]}$ . Also in Fig. 3, we have presented histograms showing the distributions of values from the emission lines considered, where Sy 1 and Sy 2 are indicated by black and red colours, respectively. We applied the two-sample Kolmogorov–Smirnov (KS) statistical test to the frequency distributions of the line ratios in Fig. 3 for the Sy 1 and Sy 2 nuclei of our sample. The KS tests show that the probability of any two distributions being taken from the same parent distribution is lower than  $10^{-5}$ , which suggests that the difference in the distributions of the density sensitive  $R_{[\text{S II}]}$  and the diagnostic emission line ratios between Sy 1 and Sy 2 is statistically significant. However, this difference does not necessarily translate into a similar significant difference in the metallicity distributions of Sy 1 and Sy 2 due to the electron density, in fact, it signifies that the electron density from

<sup>6</sup>The critical density values for  $[\text{S II}]\lambda 6716$  and  $[\text{S II}]\lambda 6731$  are  $10^{3.2}$  and  $10^{3.6} \text{ cm}^{-3}$ , respectively, see Vaona et al. (2012).

<sup>7</sup>It is worthwhile to note that only the calibration by **SB98f1** considers electron density in the formalism given by equation (11).

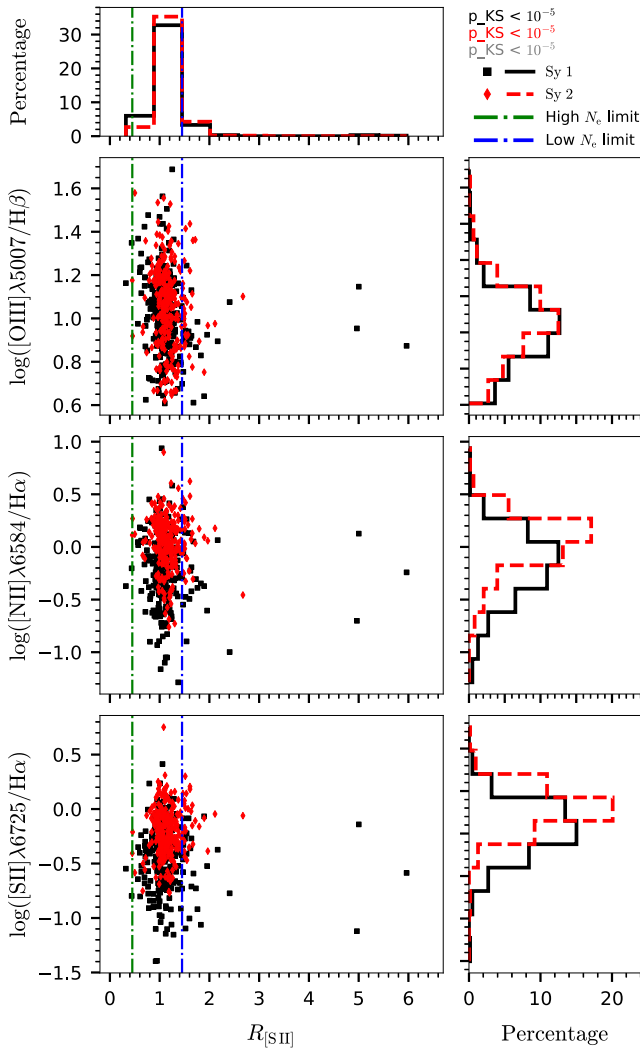


**Figure 3.** Bottom panel: The distribution of logarithmic of the diagnostic  $[S\text{ II}](\lambda\lambda 6717 + 31)/H\alpha$  versus the  $[S\text{ II}]\lambda\lambda 6717, 6731$  doublet flux ratio ( $R_{[S\text{ II}]}$ ) estimated from 287 Sy 1s and 274 Sy 2s. The green and blue dash-dotted lines represent the minimum and maximum flux ratios corresponding to the theoretical high- and low-density limits (see Section 3.1.2), respectively. Histograms of  $\log([S\text{ II}]\lambda 6725/H\alpha)$  and  $R_{[S\text{ II}]}$  are plotted in the right panel. Middle panel: Same as bottom panel but for  $\log([N\text{ II}]\lambda 6584/H\alpha)$  versus  $R_{[S\text{ II}]}$ . Top panel: Same as bottom panel but for  $\log([O\text{ III}]\lambda 5007/H\beta)$  versus  $R_{[S\text{ II}]}$ . Black and red points with corresponding coloured  $p$ -values denote Sy 1 and Sy 2 sources respectively, while the grey coloured  $p$ -value is obtained from the combined data set.

$R_{[S\text{ II}]}$  has no effect on any discrepancy which may arise from the metallicities between Sy 1 and Sy 2. The KS test values (black, red, and grey coloured  $p$ -values are for Sy 1, Sy 2, and the combined data set, respectively) from all the diagnostics, shown in Fig. 3, are lower than  $10^{-5}$  therefore the electron density has no significant effect on the metallicity values derived.

We derived electron density values from Sy 1s and Sy 2s in the range  $100 \lesssim N_e(\text{cm}^{-3}) \lesssim 2000$ , with median values of  $\sim 480 \text{ cm}^{-3}$  and  $\sim 390 \text{ cm}^{-3}$ , respectively (see Fig. 4).

### 3.1.3 Carvalho et al. (2020) calibration

Carvalho et al. (2020, hereafter C20) presented a comparison using photoionization model predictions built with the CLOUDY code (Fer-

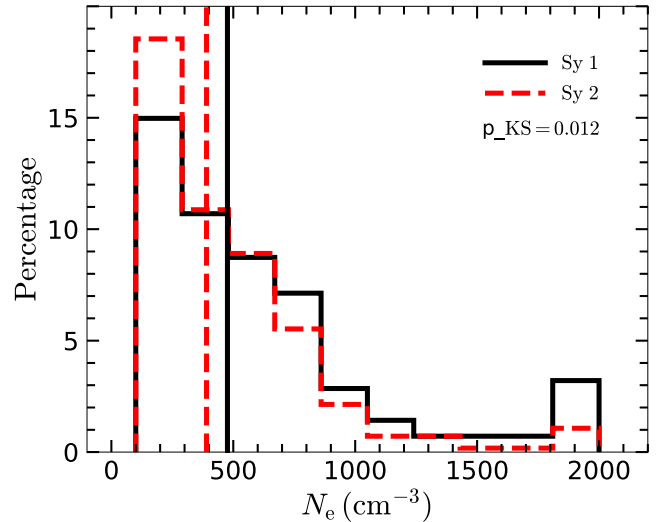


**Figure 4.** The distribution of electron density estimated from 287 Sy 1s and 274 Sy 2s of the  $[S\text{ II}]\lambda\lambda 6717, 6731$  doublet line ratio of our local samples using PYNEB code (Luridiana et al. 2015). The electron density is uniformly distributed between Sy 1s and Sy 2s except for few outliers. The median values of  $\sim 480 \text{ cm}^{-3}$  and  $\sim 390 \text{ cm}^{-3}$  for Sy 1 and Sy 2 are denoted by the solid black and dashed red vertical lines, respectively.

land et al. 2017), considering a wide range of nebular parameters, and a  $[O\text{ III}]\lambda 5007/[O\text{ II}]\lambda 3727$  versus  $[N\text{ II}]\lambda 6584/H\alpha$  diagram obtained from observational data of 463 Seyfert 2 nuclei ( $z \lesssim 0.4$ ). From this comparison, these authors derived a semi-empirical calibration between the  $N2 = \log([N\text{ II}]\lambda 6584/H\alpha)$  line ratio and the metallicity  $Z_{\text{NLR}}$ , given by

$$(Z_{\text{NLR}}/Z_{\odot}) = (4.01 \pm 0.08)^{N2} - 0.07 \pm 0.01, \quad (12)$$

which is valid for  $0.3 \lesssim (Z_{\text{NLR}}/Z_{\odot}) \lesssim 2.0$ . The metallicity results obtained from equation (12) can be converted to oxygen abundance via the relation,

$$12 + \log(O/H)_{\text{C20}} = 12 + \log[(Z_{\text{NLR}}/Z_{\odot}) \times 10^{\log(O/H)_{\odot}}], \quad (13)$$

where  $\log(O/H)_{\odot} = -3.31$  is the solar oxygen abundance value taken from Allende Prieto, Lambert & Asplund (2001). The  $N2$  index has an advantage over other metallicity indicators such as  $[N\text{ II}]\lambda 6584/[O\text{ II}]\lambda 3727$  because it involves emission lines with very close wavelengths: thus,  $N2$  is not strongly affected by dust extinction and uncertainties produced by flux calibration (Marino et al. 2013; Castro et al. 2017).

## 4 RESULTS AND DISCUSSION

### 4.1 Electron density effect

Since the SB98f1 calibration depends on the electron density, as shown above (see Section 3.1.1), it is important to analyse the potential impact of the electron density on our metallicity results.

The observed forbidden lines from the NLRs are indicative of a low density and are very useful to measure several physical parameters of the region, such as temperature and electron density. In order to examine the distributions of the electron density between Sy 1 and Sy 2, we used a two-sample KS test, as shown in Fig. 4. We find that the significant difference between the samples with the  $p$ -value,  $p_{\text{KS}} \sim 0.012$ , indicates that Sy 1 and Sy 2 are from different distribution for a confidence level of 95 per cent, although,

the same ionization mechanism is responsible for the trends between the electron density distributions of Sy 1 and Sy 2. Our derived aforementioned electron density values (see Section 3.1.2) are more in agreement with the typical densities in the NLRs of Seyferts ( $N_e \lesssim 10^4 \text{ cm}^{-3}$ ; e.g. Osterbrock & Ferland 2006; Ho 2008).

From the unified model scheme, the narrow forbidden and permitted emission lines in Sy 1 and Sy 2 sources come from the NLR, a region well outside the BLR, spanning a few tens of pc to about 1 kpc (Antonucci 1993). The mere presence of forbidden lines in the NLR indicates that the gas densities are lower than in the BLR. However, the electron density distribution in Fig. 4 shows that Sy 1 still exhibits slightly higher electron density (also see Peterson et al. 2013) in comparison to Sy 2 (Sy 1 dominates the density distribution at  $N_e > 600 \text{ cm}^{-3}$ , and vice versa), suggesting that the Sy 1 and Sy 2 are not only a geometrical phenomenon but sources with different physical properties (see Audibert et al. 2017, for other examples). It is noteworthy to emphasize that the  $N_e$  values from both Sy 1s and Sy 2s are lower than the critical density ([S II] $\lambda$ 6717:  $N_c \sim 10^{3.2} \text{ cm}^{-3}$  and [S II] $\lambda$ 6731:  $N_c \sim 10^{3.6} \text{ cm}^{-3}$ ; see Vaona et al. 2012) for the emission lines involved in the derivation of the electron density in this work therefore collisional de-excitation effect has no influence on our abundance estimates (e.g. Osterbrock & Ferland 2006; Vaona et al. 2012). It is worth mentioning that similar trends are found even using higher ionization potential lines, such as [Ar IV] $\lambda$ 4711,  $\lambda$ 4740 (Vaona et al. 2012; Congiu et al. 2017; Cerqueira-Campos et al. 2021).

Additionally, the electron density determined from the  $R_{[\text{S III}]}$  is much lower than those obtained using auroral and transauroral lines, as well as ionization parameter based approach (e.g. Davies et al. 2020). Furthermore, even considering the highest  $N_e$  value we assumed for  $R_{[\text{S III}]}$   $\lesssim 0.45$  ( $N_e = 2000 \text{ cm}^{-3}$ ), the O/H correction is  $\sim 0.1$  dex, which is in order of the uncertainty of abundances via direct measurements of the electron temperature (e.g. Kennicutt, Bresolin & Garnett 2003; Hägele et al. 2008) and even lower than those ( $\sim 0.2$  dex) via strong line methods (e.g. Denicoló et al. 2002; Marino et al. 2013). Thus, the abundances derived from our sample are only marginally influenced by the electron density.

The NLR can be explained by high-density gas clouds transfer from the nuclear region to the outer part in the host galaxy through the outflows driven by the AGN as shown by photoionization models (e.g. Wada, Yonekura & Nagao 2018), implying that the NLR gas density increases toward small radii (e.g. Bennert et al. 2006a,b). For instance, spatially resolved observational studies of the NLRs have revealed a profile of electron density along the AGN radius, i.e. electron densities ranging from  $\sim 2500 \text{ cm}^{-3}$  at the central parts to  $\sim 100 \text{ cm}^{-3}$  at the outskirts (e.g. Congiu et al. 2017; Freitas et al. 2018; Kakkad et al. 2018; Revalski, Crenshaw & Kraemer 2018; Mingozzi et al. 2019). Since our spectra were integrated in the central parts of the galaxies, the electron density values obtained in the present work must be considered as mean values for the NLRs. The existence of the density effect has already been taken into account in the strong-line calibration by C20, while SB98f1 has proposed a correction (equation 11), which is valid for the gas density in the range  $10^2 \lesssim N_e(\text{cm}^{-3}) \lesssim 10^4$ , and would have a maximum impact of 0.1 dex (e.g. Dors 2021) on the metallicity correction. While the use of  $R_{[\text{S III}]}$  is still a subject of ongoing debate (e.g. Shimizu et al. 2019; Davies et al. 2020; Nicholls, Kewley & Sutherland 2020), it is still better suited to probe the NLR gas density for the proposed correction by SB98f1. Finally, even electron density values derived from spatially observed AGNs and from emission lines emitted by ions (e.g.  $\text{Ar}^{3+}$ ) with higher ionization potentials than  $\text{S}^+$  support the phenomenon that the NLR is indicative of a low density regime ( $N_e \lesssim 10^4 \text{ cm}^{-3}$ ). Thus, collisional de-excitation has a minimum

effect on the formation of the emission lines we used to estimate the metallicity (e.g. [O III] $\lambda$ 5007:  $N_c \sim 10^{5.8} \text{ cm}^{-3}$  and [N II] $\lambda$ 6584:  $N_c \sim 10^{4.9} \text{ cm}^{-3}$ ; see Vaona et al. 2012).

## 4.2 Caveats for the Seyfert 1 metallicity

As widely accepted in the AGNs phenomena (e.g. Antonucci 1993), two distinct emission-line regions are expected to exist around the accretion disc: (i) A BLR, which consists of relatively dense clouds ( $N_e \gtrsim 10^5 \text{ cm}^{-3}$ ) and highly perturbed gas. In this region forbidden emission lines are suppressed by collisional de-excitation while broad permitted lines are emitted with FWHM  $\gtrsim 1000 \text{ km s}^{-1}$ , and (ii) the NLR with low electron density clouds ( $N_e \lesssim 10^4 \text{ cm}^{-3}$ ) where the narrow forbidden and permitted emission lines (FWHM  $\lesssim 1000 \text{ km s}^{-1}$ ) are produced.

Despite these two distinct regions, some studies have shown that, at least in some Sy 1 nuclei, some forbidden lines can also be emitted near the BLRs or, in other words, the NLRs present very high electron density values. Peterson et al. (2013) used observational data from the International AGN Watch campaign via the Hubble Space Telescope, found a variability of the flux of [O III] $\lambda$ 5007 and the continuum ( $\lambda = 5100 \text{ \AA}$ ) in the well-studied Seyfert 1 NGC 5548. These authors (see also Zhang & Feng 2016; Sergeev, Nazarov & Borman 2017; Landt et al. 2019; Horne et al. 2021) showed that the [O III] emission occurs preferentially in a compact NLR (1–3 pc) with an electron density  $\sim 10^5 \text{ cm}^{-3}$ , which is close to the critical density for this line ( $10^{5.8} \text{ cm}^{-3}$ ; Vaona et al. 2012). This scenario precludes any direct electron density estimation in the gas region where most of the [O III] is emitted, even using the [Ar IV] line ratio.

Since SB98f1 and C20 calibrations were obtained based on photoionization models assuming low ( $\lesssim 10^3 \text{ cm}^{-3}$ ) and constant electron density values along the AGN radius, we can have some biases in the Seyfert 1 oxygen abundance estimates. In order to verify the possible effect of high-density clouds on the strong emission lines used in our metallicity estimates, we performed photoionization model simulations following a similar procedure adopted by Dors et al. (2019). We used AGN models, which were built from version 17.00 of the spectral synthesis code CLOUDY (Ferland et al. 2017), with radial density profiles  $N_e \propto r^{-0.5}$ , where  $r$  is the distance to the center of the AGN, as derived observationally from the Sy 2 galaxy Mrk 573 by Revalski et al. (2018). We assumed the same nebular parameters used by C20 but for metallicity ( $Z/Z_\odot$ ) = 0.2, 1.0, 2.0, an innermost radius of 0.1 pc, the outermost radius where the gas temperature reaches 4000 K (standard value in the CLOUDY code), logarithm of the number of ionizing photons emitted by the central source is considered to be  $\log[Q(\text{H})] = 54$ , the slope of the spectral energy distribution,  $\alpha_{\text{ox}} = -1.1$  and  $\log(N_e)$  ranging from 3 to 7 with a step of 1.0 dex. In Fig. 5, the predicted intensities of [O III] $\lambda$ 5007/H $\beta$ , [N II] $\lambda$ 6584/H $\alpha$  emission line ratios versus the  $\log(N_e)$  are shown. Also in this figure the critical density values for [N II] $\lambda$ 6584 and [O III] $\lambda$ 5007 are indicated. It can be seen that the variations in electron density, for density values lower than the critical density ( $N_c$ ), have practically insignificant effects on the emission line ratios considered for our metallicity estimations, thus validating the employed metallicity methodology for the Sy 1 sources.

It is worth mentioning that the application of strong emission line calibrations to the derivation of metallicity must be considered in a statistical analysis considering a large object sample, as performed in this work. Obviously, estimates based on detailed photoionization models which take into account a wide spectral wavelength range, as performed by Kraemer et al. (1994) for the two Sy 2 galaxies



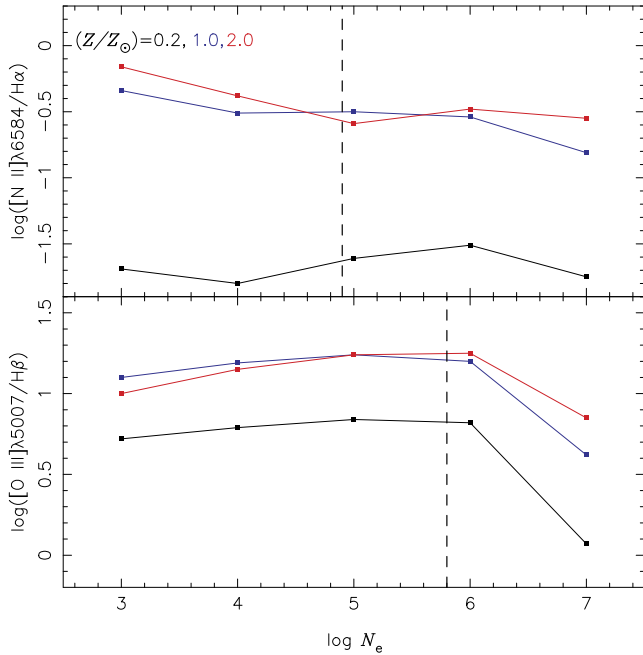


**Figure 5.** The intensities of  $[O\ III]\lambda 5007/H\beta$  and  $[N\ II]\lambda 6584/H\alpha$  emission line ratios versus the logarithm of the electron density predicted by photoionization models assuming radial density profiles  $N_e \propto r^{-0.5}$ , where  $r$  is the distance to the centre of the AGN. Solid lines connect the points representing model predictions with different metallicities, as indicated. Dashed lines represent the critical density values of  $10^{4.9}\text{ cm}^{-3}$  and  $10^{5.8}\text{ cm}^{-3}$  for  $[N\ II]\lambda 6584$  and  $[O\ III]\lambda 5007$  (Vaona et al. 2012), respectively.

NGC 7674 and IZw 92, produce more precise metallicity values, but such results are available from a few objects.

### 4.3 Gas phase abundances

In Fig. 6(a), we show the distribution of oxygen abundances in this study estimated from the NLRs of 287 Sy 1s and 274 Sy 2s with respect to the calibrations by SB98f1 and C20 (blue lines for Sy 1 and red for Sy 2). We also show a KS test  $p$ -values as follows: (i) for Sy 1 sources comparing the two different methods:  $p_{\text{KS}}(\text{Sy } 1) < 10^{-5}$ ; (ii) for Sy 2 sources comparing the two different methods:  $p_{\text{KS}}(\text{Sy } 2) < 10^{-5}$ ; (iii) comparing Sy 1 and Sy 2 abundances using the SB98f1 method:  $p_{\text{KS}}(\text{SB98f1}) < 10^{-5}$  and, (iv) comparing Sy 1 and Sy 2 abundances using the C20 method:  $p_{\text{KS}}(\text{C20}) < 10^{-5}$ .

It is clear that the O/H distribution from Sy 1 covers a wide range of metallicities as compared to Sy 2, with Sy 1 sources showing median values ( $8.44 \pm 0.03$  for SB98f1 and  $8.55 \pm 0.04$  for C20) lower than those in type 2 objects ( $8.54 \pm 0.02$  for SB98f1 and  $8.70 \pm 0.02$  for C20). This difference is interpreted as different chemical enrichment paths for type 1 and type 2 sources. This could be due to a more active previous star-formation in the type 2 sources than in type 1s, thus enriching the interstellar medium (ISM) with recycled material from stellar evolution. In this hypotheses, the AGN would be quenching the star-formation in the nuclear region of type 1 sources. Another possible scenario would be that type 1 sources are experiencing an inflow of low metallicity gas that is diluting the richer gas available in the centre of the galaxies, making the overall abundance lower in type 1 sources. Indeed this hypothesis is in agreement with the findings by N22 when studying the abundances radial profiles of a sample of Sy 2 sources and comparing them with the nuclear region

(e.g. the disc extrapolated values are higher than those obtained for the nuclear region).

To compare our results with the literature, in Fig. 6(b), we show the distribution of the gas phase abundance estimates for the Sy 2 galaxies in this study in comparison with similar estimations by do Nascimento et al. (2022, hereafter N22) using observational data from the SDSS-IV MaNGA survey. In addition we also performed KS tests to compare both samples, as follows: (i) comparison between our results and those from N22 using the SB98f1 method:  $p_{\text{KS}}(\text{SB98f1}) < 10^{-5}$ ; (ii) comparison between our results and those from N22 using the C20 method:  $p_{\text{KS}}(\text{C20}) < 10^{-5}$  and, (iii) a comparison between the results found by N22 from the MaNGA Sy 2 sources using the two different calibrations (SB98f1 and C20):  $p_{\text{KS}}(\text{N22}) = 0.004$ . We observe that there is a good agreement between our estimates and those obtained by N22 from the two different calibrations. However, comparing the results from Sy 2s using the two calibrations we notice that there is a slight difference, which is obvious in the KS  $p$ -values [ $p_{\text{KS}}(\text{Sy } 2) \times p_{\text{KS}}(\text{N22})$ ] between our estimates and those obtained by N22, but the difference is not statistically significant.

## 4.4 Oxygen abundance and AGN properties

### 4.4.1 X-ray luminosity

In this section we compare the X-ray luminosities with the oxygen abundances determined for the 561 sources using the different calibrations (see Section 2.2). In Figs 7 and 8, we show the the  $L_X$ - $Z_{NLR}$  relations which indicate anticorrelations between the X-ray luminosities (observed and intrinsic, respectively) and metallicities from the NLR. The solid grey lines show the linear relation between the two parameters ( $L_X$  and  $Z_{NLR}$ ). These lines were obtained following Riffel et al. (2021) using 1000 bootstrap realizations (Davison & Hinkley 1997) with Huber Regressor model that is robust to outliers (Owen 2007). The Pearson correlation coefficients and  $p$ -values are quoted (they are the mean value of the bootstrap realizations). We also average the oxygen abundance values in bins of 0.5 dex of  $L_X$ , which are shown in red, and a liner regression (red dashed line) fit was performed over them (removing the points which are the average of a small number of objects – shown in magenta). We notice that the metallicity estimates show a dependence on the various X-ray luminosities, as seen from the Pearson correlation  $p$ -values. In addition, there is a higher correlation from the calibration by C20 ( $r = -0.27 \pm 0.04$ ;  $-0.22 \pm 0.04$ ) in comparison with SB98f1 ( $r = -0.24 \pm 0.04$ ;  $-0.20 \pm 0.05$ ) at both the observed ( $\log L_{2-10}^{\text{obs}}$ ) and intrinsic ( $\log L_{14-150}^{\text{int}}$ ) X-ray luminosities. At this point, it is difficult to reconcile which physical quantity is responsible for the observed correlation difference. However, the metallicity exhibits somewhat dependence on the X-ray luminosity regardless of the method used (also see Oh et al. 2017), indicating that there may be a common physical driving mechanism. It is important to highlight that we tested for the correlations separating type 1 and type 2 sources, as a result of this exercise, we note that the metallicity estimates from Sy 1 and Sy 2 follow the same trend with respect to  $L_X$  (e.g. the  $r$  values are the same within the margin of error).

### 4.4.2 The mass–metallicity relation

The inflows of metal-poor gas which activate the star formation and dilute the metallicity of the ISM or the outflows of metal-rich gas which stop the star formation are some mechanisms which depend on MZR. In Figs 9 and 10, we plot the metallicity as a function of the

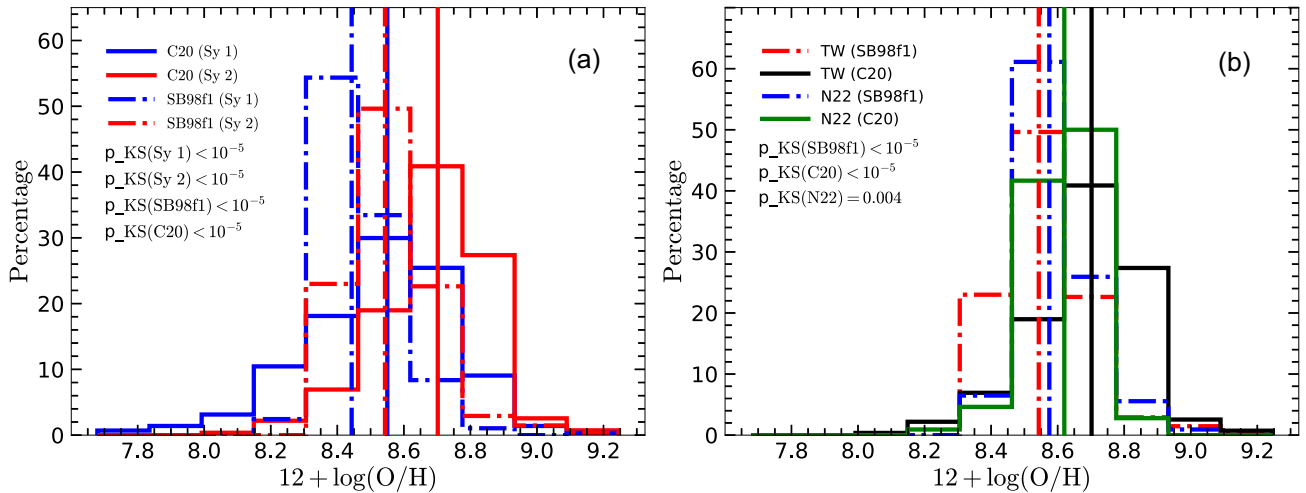


**Figure 6.** Panel (a): distribution of oxygen abundances in this study estimated from the NLR of 287 Sy 1s and 274 Sy 2s using the calibrations by **SB98f1** and **C20**. The blue dash-dotted and red solid vertical lines represent the median values of each histogram (i.e. the same colour and line pattern are used for the histogram and median value). Panel (b): Distribution of oxygen abundances in this study for the 274 Sy 2s and 108 Sy 2s estimated by **N22** using the **SB98f1** (red and blue) and **C20** (black and green) calibrations. A two-sample KS statistical test  $p$ -values are also shown for each calibration as well as a comparison between the SDSS-IV MaNGA survey and BASS DR2 data sets. For completeness we quote the value of  $12 + \log(\text{O}/\text{H})_{\odot} = 8.69$  for the solar abundance derived by Allende Prieto et al. (2001).

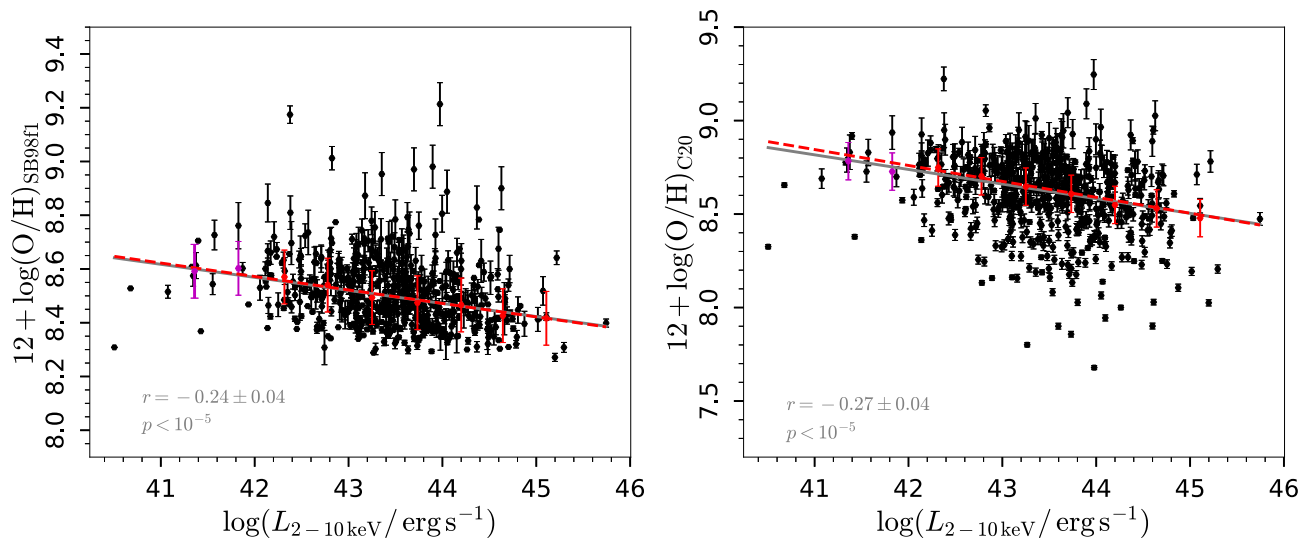


**Figure 7.** Metallicity versus observed ( $\log L_{2-10}$ ) luminosity using the strong-line calibrations by **SB98f1** and **C20**. The grey correlation parameters correspond to the solid grey lines, which represent the linear fits to the black points. The red points and dashed line represent average oxygen abundance values in bins of 0.5 dex of  $L_X$  and line of best fit to the red points, respectively.

black hole mass and the host stellar mass for individual galaxies in the sample, respectively. The MZR has been shown to be dependent on redshift and various galaxy properties in the NLRs of AGNs (Matsuoka et al. 2018) and other SFs (e.g. Kewley & Ellison 2008; Huang et al. 2019; Curti et al. 2020). It has generally been shown that, at a given stellar mass, lower redshift galaxies have higher gas-phase metallicities than their higher redshift counterparts, while the MZR always shows a positive correlation. In Fig. 9, we investigate the redshift evolution of the MZR between the metallicities and the black hole mass. We found weak correlations ( $r = 0.12$ ;  $p = 0.05$ , for **SB98f1** and  $r = 0.09$ ;  $p = 0.15$  for **C20** across the full redshift range  $z \lesssim 0.31$ ), which is consistent with the findings by Oh et al. (2017), who found a weak correlation of the  $[\text{O III}]/\text{H}\beta$  line ratio with the SMBH mass. We show the distribution of the NLR

metallicities as a function of the stellar masses of the hot galaxies in Fig. 10. We find positive correlations between NLR metallicities and the stellar masses at three different redshifts bins. This implies that the gas-phase metallicities in the NLRs of AGNs are connected to the properties of the hot galaxies.

The MZR and FMRs have widely been investigated in SFs but such relations have rarely been found in AGNs. However, the origin of the MZR and FMRs remain active research in astrophysics. Therefore, we further test this hypothesis by comparing the oxygen abundances values computed here with those obtained in star forming galaxies. A direct comparison between findings using samples from the same source might not reveal the actual properties which influence the MZR, as we have demonstrated above. Therefore, it is important to show a comparison between our results and other

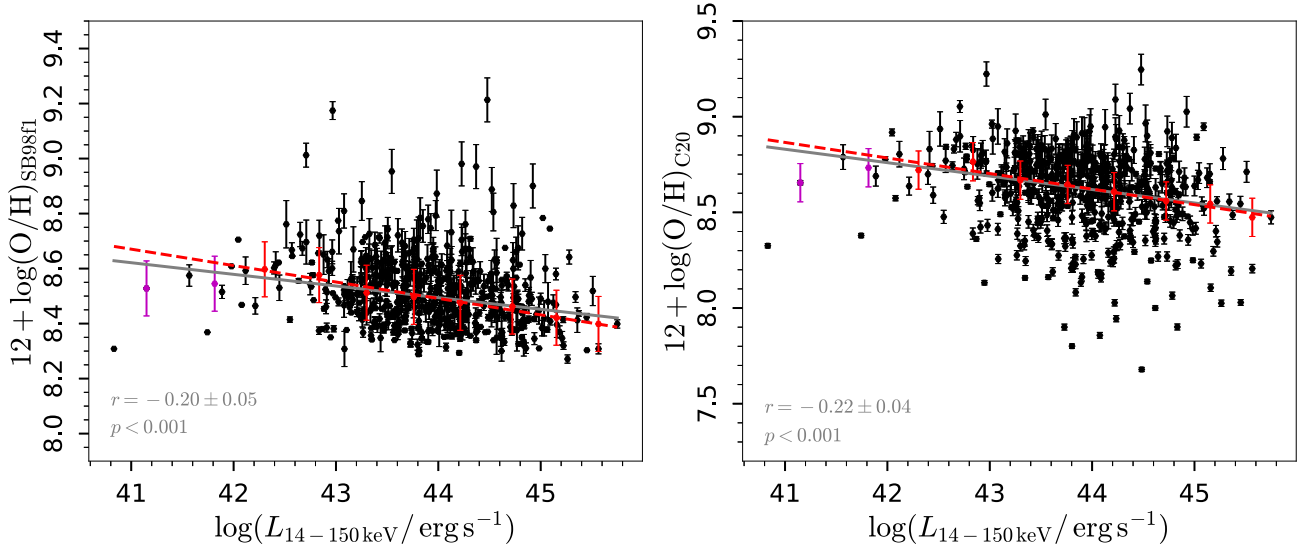


Figure 8. Same as Fig. 7 but for the metallicity versus intrinsic ( $L_{14-150}$ ) luminosity.

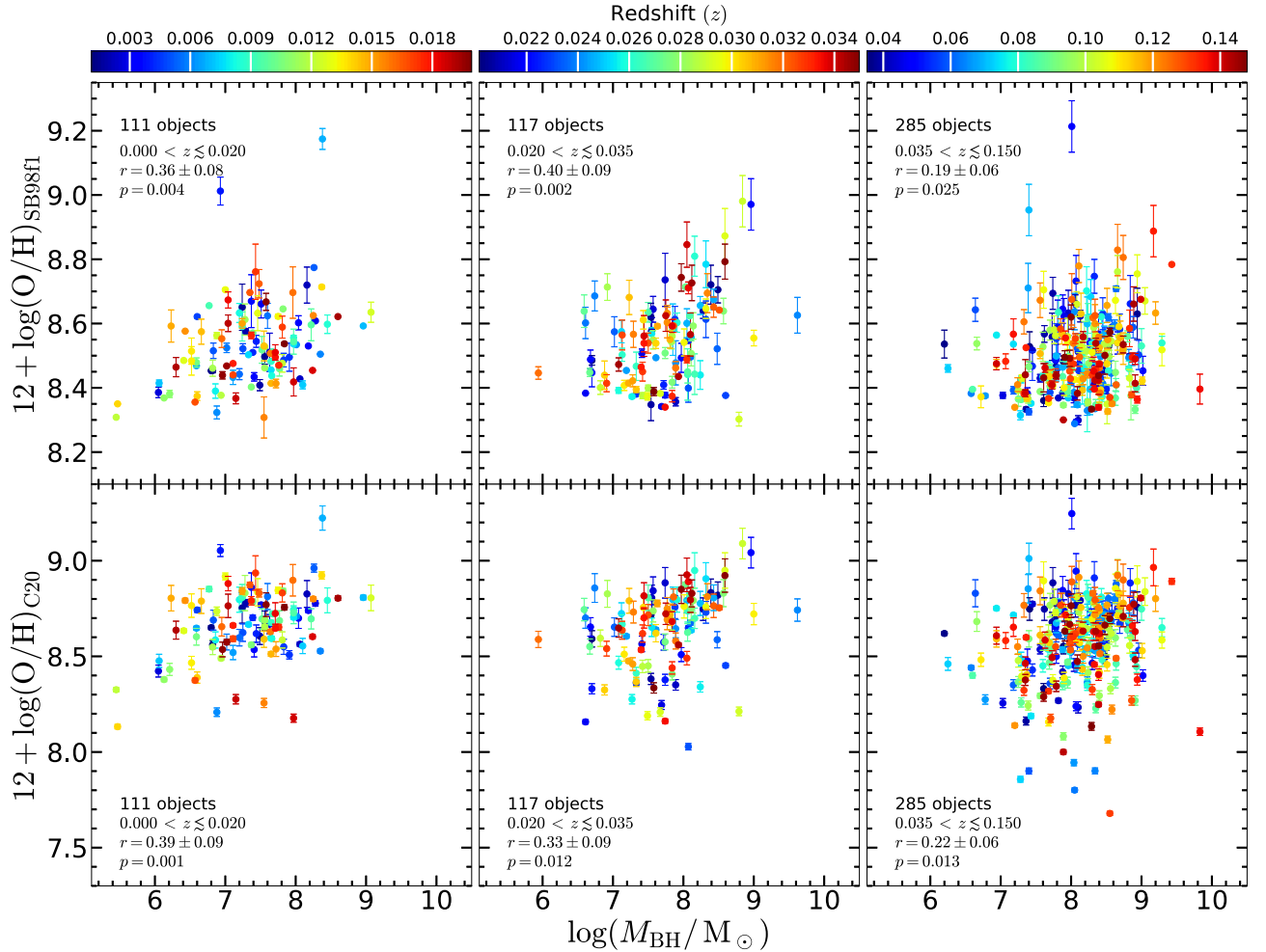
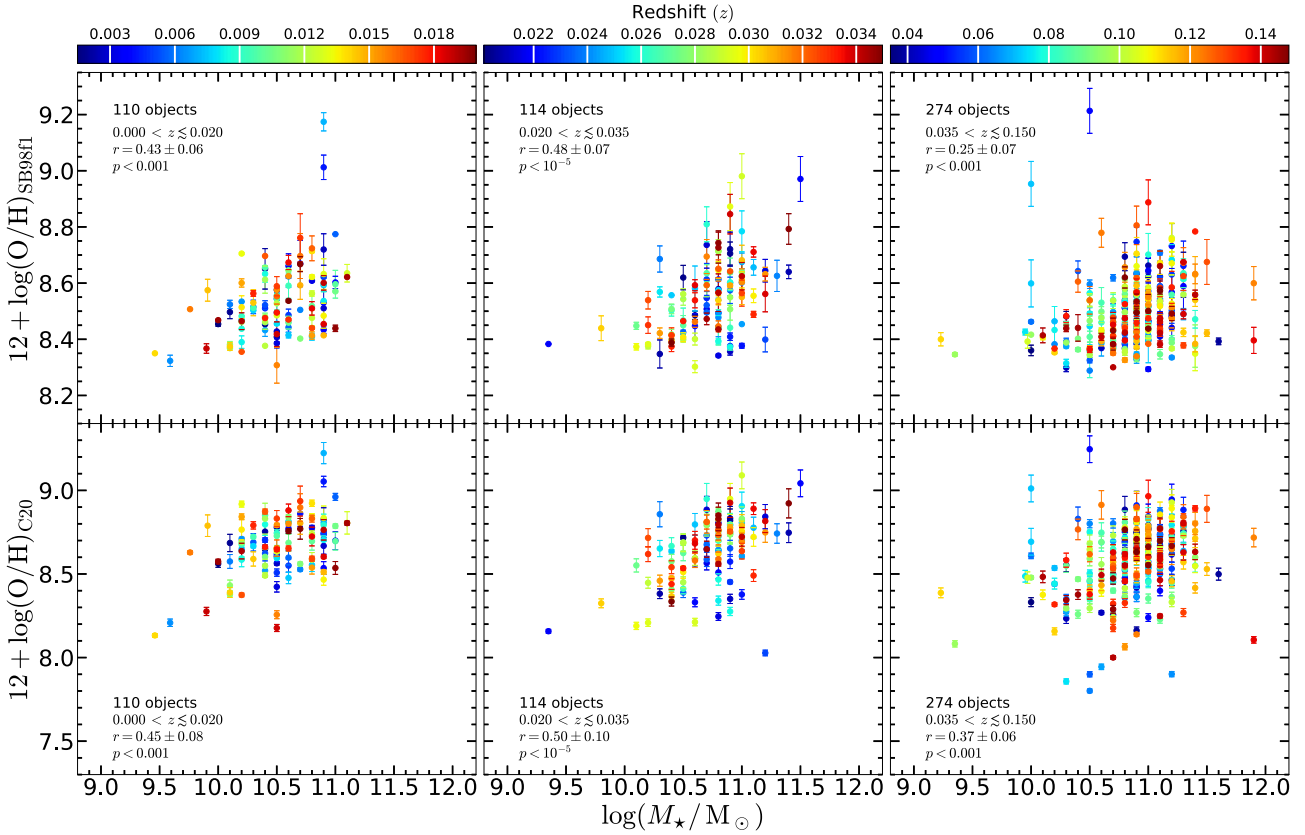


Figure 9. Bottom panels: The mass–metallicity relations between the black hole mass and the metallicity from the calibration by C20. Top panels: Same as bottom panels but for the calibration by SB98f1. The points in all panels are colour coded by redshift, as indicated by the colour bar. The number of sources is the same in the corresponding bottom and top panels. The results from the correlation analysis in redshift bins ( $0.000 < z \leq 0.020$ ,  $0.020 < z \leq 0.035$  and  $0.035 < z \leq 0.150$ ) are indicated in each panel. There is no correlation parameters at  $z > 0.15$ .



**Figure 10.** Same as Fig. 9 but for the stellar mass of the host galaxies.

findings from the literature. We briefly highlight some of the MZR from the literature in the following.

We considered the first MZR by Tremonti et al. (2004), who used SDSS spectroscopic data to demonstrate the MZR with  $\sim 0.1$  dex scatter at  $z \sim 0.1$  considering stellar masses in the range  $8.5 \lesssim \log(M_*/M_\odot) \lesssim 11$ . We also took into consideration the MZR at  $z \sim 0.07$  derived by Kewley & Ellison (2008) based on the calibration by Kobulnicky & Kewley (2004). Additionally, Matsuoka et al. (2018) found the MZR for type-2 AGNs at  $z \sim 3.0$ , using high- $z$  radio galaxies and X-ray selected radio-quiet AGNs. Furthermore, Huang et al. (2019) used the composite spectra of galaxies from the extended Baryon Oscillation Spectroscopic Survey of the Sloan Digit Sky Survey (SDSS IV/eBOSS) with a median redshift of  $\sim 0.83$ . They found a redshift evolution of the MZR described by the relation,

$$12 + \log(\text{O}/\text{H}) = Z_0 + \log \left[ 1 - \exp \left( - \left[ \frac{M_*}{M_0} \right]^\gamma \right) \right] \quad (14)$$

where  $Z_0 = 8.977$ ,  $\log M_0 = 9.961$ , and  $\gamma = 0.661$  for the redshift range 0.60–1.05 with the stellar mass covering the range  $9 < \log(M_*/M_\odot) < 12$ . Finally, Curti et al. (2020) parametrized the median MZR via the relation,

$$12 + \log(\text{O}/\text{H}) = Z_0 - \frac{\gamma}{\beta} \log \left( 1 + \left( \frac{M}{M_0} \right)^{-\beta} \right) \quad (15)$$

where  $Z_0 = 8.793$  is the asymptotic metallicity at high  $M_*$ ,  $\log(M_0/M_\odot) = 10.02$  is the turnover mass below which the MZR reduces to a power law of index  $\gamma = 0.28$  and  $\beta = 1.2$  is a measure of how fast the relation reach the asymptotic value.

In Fig. 11, we show the redshift evolution of the MZR in terms of the metallicities and the stellar mass of the host galaxies in this work

as well as a comparison with similar MZR from the literature. The comparison among previous studies of SFs in Fig. 11 show a unique MZR downward evolution trend from  $z \sim 0.07$  (Kewley & Ellison 2008),  $z \sim 0.1$  Tremonti et al. (2004),  $z \sim 0.83$  Huang et al. (2019), to  $z > 0.027$  Curti et al. (2020), which is consistent with the fact that as redshift increases, the MZR shifts downward, indicating that more evolved galaxies tend to be more metal-rich (e.g. Maiolino et al. 2008; Huang et al. 2019). Similarly, a comparison between our result at a median redshift of  $z \sim 0.04$  and the MZR derived by Matsuoka et al. (2018) for AGNs at  $z \sim 3$  follow the same downward trend. The X-ray selected AGNs have reveal the redshift evolution of the  $M_*$ – $Z_{\text{NLR}}$  relations, which is consistent with the findings by Matsuoka et al. (2018) and other star-forming galaxies (e.g. Huang et al. 2019; Sanders et al. 2021). We note that the origin of the differences between the MZR is outside the purview of this study. However, we highlight some possible scenarios which could be attributed to the differences in MZR between SFs and AGNs. Comparing our results with those by Matsuoka et al. (2018, for AGN with  $z \sim 3$ ), we find that the curves from our sample is more flat and that the values are on average  $\sim 0.3$  dex higher than those estimated from higher redshift sources. We interpret this as the redshift evolution of MZR in AGNs, in the sense that metal-rich gas are usually found in the more evolved galaxies. However, when comparing the mean values obtained from SF galaxies, reported by Tremonti et al. (2004, red line), Kewley & Ellison (2008, magenta line), Huang et al. (2019, teal line), and Curti et al. (2020, black line) in the stellar mass range of our sample (see Fig. 11), it can be seen that our AGN hosts (dashed cyan and blue lines) do present values that are 0.2–0.5 dex lower than SF galaxies (solid lines). We note that different metallicity calibrations, even when based on the same diagnostics, are typically not consistent with

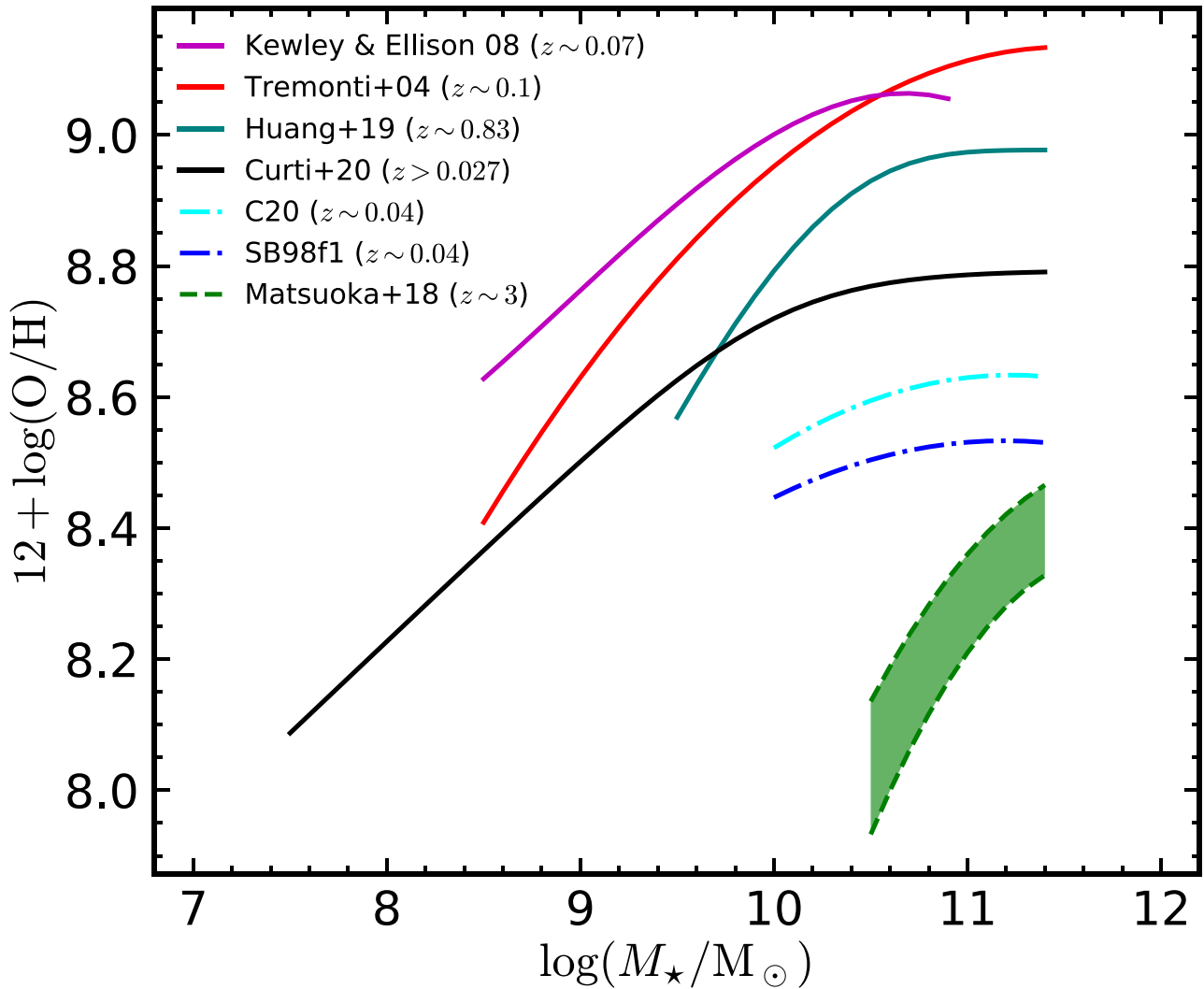


**Figure 11.** Comparison between the mass–metallicity relations of the BASS sample (with a median redshift at  $z \sim 0.04$ ) and from the literature. The solid magenta, red, teal and black curves denote the MZR for star-forming galaxies at  $z \sim 0.07$ ,  $z \sim 0.1$ ,  $z \sim 0.83$ –, and  $z > 0.027$  derived by Kewley & Ellison (2008), Tremonti et al. (2004), Huang et al. (2019), and Curti et al. (2020), respectively. The dash–dotted cyan and blue curves represent our estimates from C20 and SB98f1 calibrations, respectively, while the green filled area is from type-2 AGNs at  $z \sim 3$  by Matsuoka et al. (2018).

one another and usually result in systematic abundance discrepancies from  $-0.09$  up to  $0.8$  dex (e.g. Kewley & Ellison 2008; Blanc et al. 2015; Bian et al. 2017; Dors et al. 2020a), which is consistent with the correlation differences between our estimates and the aforementioned previous results obtained from SFs and AGNs. This discrepancy can not, however, be associated with the redshift evolution of the MZR, since the sources studied here are in the lower redshift range (see Fig. 11) with different ionization mechanisms from SFs, thus, it indicates that AGNs and SF galaxies have different chemical evolution paths, suggesting that the abundances of AGN hosts are somehow affected by the central engine.

In fact, the SF around SMBH may be affected in many aspects (as a consequence of the abundances too). For example, while some studies associate the AGN outflows with the suppression of the SF (e.g. Granato et al. 2004; Fabian 2012; King & Pounds 2015; Zubovas & Bourne 2017; Trussler et al. 2020) other studies suggest that these outflows and jets can compress the galactic gas, thus acting as a catalyzer and boosting the SF (e.g. Rees 1989; Hopkins 2012; Nayakshin & Zubovas 2012; Bieri et al. 2016; Zubovas et al. 2013;

Zubovas & Bourne 2017) and even form stars inside the outflow (e.g. Ishibashi & Fabian 2012; Zubovas et al. 2013; El-Badry et al. 2016; Wang & Loeb 2018; Gallagher et al. 2019). Using high spatial resolution observations taken with adaptive-optics assisted integral field spectroscopy Riffel et al. (2022, see also references therein) have shown that, once the AGN is triggered, it precludes further SF, in the sense that it can be associated with the lack of new star formation in the inner few hundred of pc of AGN hosts. N22 studied spatial variation of oxygen abundances on a sample of AGN, and has suggested that the drop in the  $O/H$  abundance in the AGN dominated region when compared with the values obtained for the disc region is due to the inflow of less metallic gas towards the central region of the galaxy. All these processes contribute to a *chaotic* chemical evolution of AGNs.

#### 4.4.3 Metallicity and accretion rate

In order to test for a possible influence of the AGN on the metallicity of the host galaxies, we have compared the metallicities with the

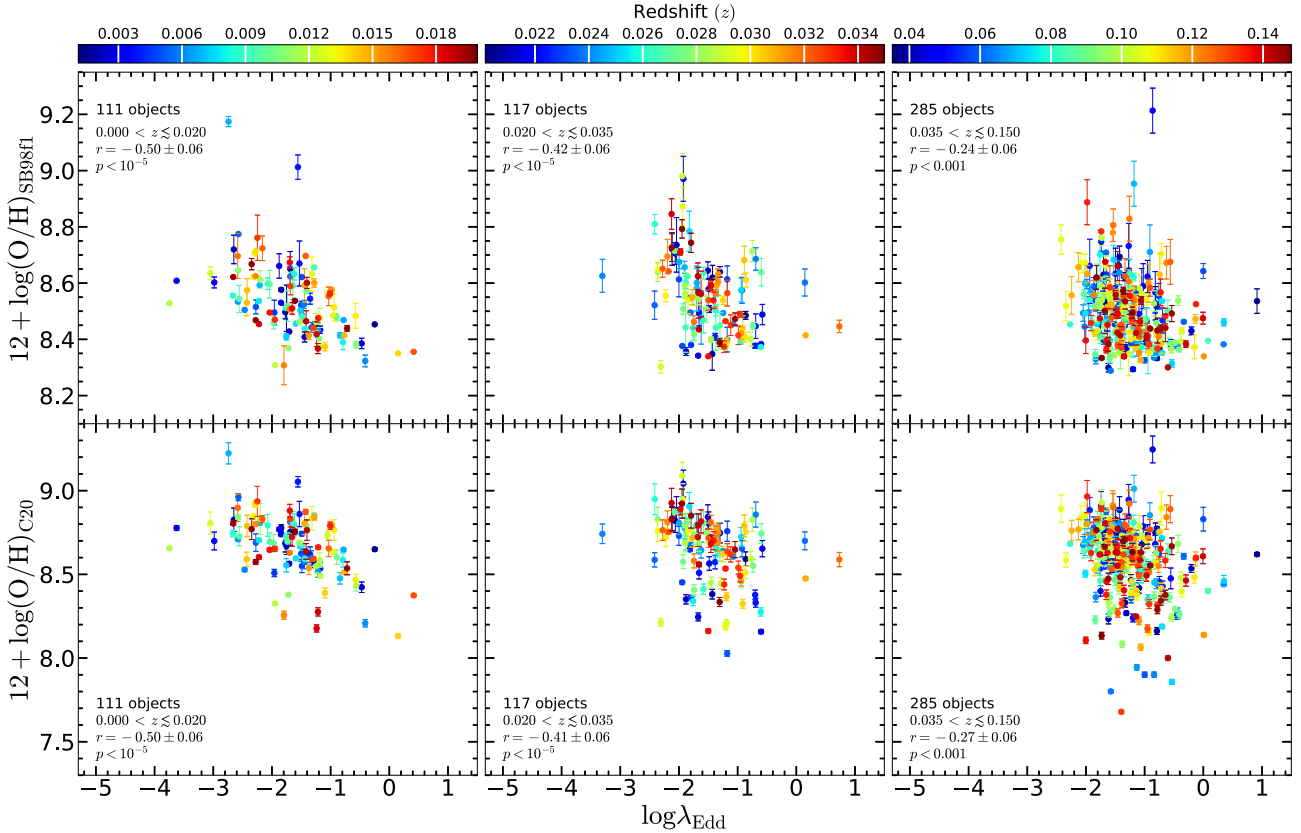


**Figure 12.** Bottom panels: The relation between the metallicity from the calibration by C20 and the Eddington ratios from the intrinsic X-ray luminosity ( $L_{14-150}$ ). Top panels: Same as bottom panels but for the calibration by SB98f1. The points in all panels are colour coded by redshift, as indicated by the colour bar. The number of sources is the same in the corresponding bottom and top panels. The results from the correlation analysis in redshift bins ( $0.000 < z \leq 0.020$ ,  $0.020 < z \leq 0.035$  and  $0.035 < z \leq 0.150$ ) are indicated in each panel. There is no correlation parameters at  $z > 0.15$ .

Eddington ratio, which is a function of luminosity and  $M_{\text{BH}}$ , shown in Fig. 12 and since there is a similar distribution on the plane  $\log \lambda_{\text{Edd}} \times \log(L_{\text{bol}})$  between Sy 1 and Sy 2 we do not discriminate between them in subsequent analysis. This assertion reiterates the fact that there are no significant variations between the SFRs of type 1 and type 2 AGNs, which is consistent with earlier findings using SFRs derived from infrared indicators (e.g. Zou et al. 2019).

Furthermore, from Fig. 12, it can be seen that there is anticorrelation between the accretion rate and the metallicity, for different redshift bins, with Pearson correlation coefficients ranging from  $r \sim -0.24$  to  $-0.50$  and  $p$ -value  $< 10^{-5}$  depending on the redshift range and the adopted calibration. These results are more in agreement with those found by Oh et al. (2017) who compared  $[\text{N II}]\lambda 6583/\text{H}\alpha$ , which is sensitive to O/H abundances, with  $\lambda_{\text{Edd}}$  for a sub-sample of the local hard X-ray-selected BAT AGNs (297 sources at  $0.01 < z < 0.40$ ) as well as at redshift beyond the local Universe (e.g. 53 sources at  $0.6 < z < 1.7$ ; Oh et al. 2019) and found a clear anticorrelation between those two quantities. Moreover, Matsuoka et al. (2011) used optical spectra of high redshift ( $2.3 < z < 3.0$ ) quasars and compared different metallicity sensitive emission line ratios with  $\lambda_{\text{Edd}}$ . They obtained mostly positive correlations<sup>8</sup> from the comparison between the metallicity sensitive line ratios and  $\lambda_{\text{Edd}}$ , as can be observed from their Fig. 6. Furthermore, they found that the  $L_{\text{AGN}}-Z_{\text{BLR}}$  trend is as a result of the positive correlations between

these same line ratios and the SMBH mass. Also, Shemmer et al. (2004, and references therein) found that in high redshift ( $2.0 < z < 3.5$ ) quasars there is a positive correlation between luminosity (or SMBH mass) and BLR metallicity sensitive line ratios (N V/C IV).

The correlation of the  $Z_{\text{NLR}}$  and/or metallicity sensitive emission line ratios with the  $L_X$ , or  $\lambda_{\text{Edd}}$  in Seyferts is in contrast with the results that were obtained based on measurements of UV broad emission lines in quasar. Additionally, the correlation of  $Z_{\text{AGN}}-M_{\text{BH}}$  relation, is extremely weak (or absent) in Seyferts as compared to quasars. These discrepancies might be due to the fact that Seyferts are moderate-luminous AGNs whereas quasars are the most-luminous AGNs as well as the different methodologies used in the estimation of the  $\lambda_{\text{Edd}}$ , which has a strong dependence on the  $L_X-M_{\text{BH}}$  relation. It is worthwhile to note that, the  $\lambda_{\text{Edd}}$  is responsible for the AGN fueling while the metal enrichment of the nuclear gas is due to nuclear/circumnuclear star-formation.

Moreover, it is challenging to fairly compare the results obtained from the BLR using high  $z$  quasars with those found from the NLR of local Universe sources. Even, to compare the NLR gas from local Universe sources with quasar is very difficult, as has been shown by Netzer et al. (2004), the NLR properties in high-luminosity quasars are very different from those observed in nearby AGNs, for example, they may be in a phase of violent star-forming events that release high quantities of metals into the gas. This would naturally explain the differences we observe between our results and those from high redshift objects. In fact, this is fully supported by our finding in Fig. 12, since the ‘strength’ of the anticorrelation (measured by the

<sup>8</sup>It is worth mentioning that depending on the line ratio and the black hole mass bins there is no correlation found in some cases.

$r$ ) drops when we consider the higher redshift sources ( $0.035 < z < 0.150$ ), indicating that there is a change in the chemical evolution path of AGNs with redshift.

The anticorrelation observed in Fig. 12, where  $\lambda_{\text{Edd}}$  increases with decreasing metallicity suggest that the chemical evolution of the host galaxy seems to be affected by the AGN activity through suppression of their nuclear SF, and thus stopping the enrichment, or the sources with higher Eddington ratio experiencing an inflow of a lower metallicity gas from the outskirts of the galaxy and/or from the cosmic web. Thus, this metal-poor gas would be diluting the more metal-rich gas in the inner regions and feeding/triggering the AGN. The scatter we observe from the  $Z_{\text{NLR}}$  in Fig. 12 (e.g. for a fixed luminosity, there is a range of possible metallicity values), could be explained by the fact that the gas reaching the SMBH is probably originating from mass loss from intermediate-age stellar population (Riffel et al. 2022). In this sense, the outskirts low metallicity gas reaching the AGN, will get an extra supply of gas that has already been processed by stellar nucleosynthesis, and thus enhancing the  $Z_{\text{NLR}}$ . Therefore, the values of oxygen abundances, for a fixed  $L_X$  would be the balance between the pristine and the processed gas phases.

From the above, we interpret the anticorrelation found in Fig. 12 as due to the combination of the inflow of pristine gas diluting the metal-rich gas, activating the AGNs, which in turn suppress the nuclear SF, thus stopping the gas enriching process. In this framework, the more luminous sources will have lower metallicities (no SF + pristine gas), while the less luminous would have higher  $Z_{\text{NLR}}$  values since they may still have some level of nuclear SF but no (or a small amount of) pristine gas is reaching their SMBHs.

## 5 CONCLUDING REMARKS

We derived metallicities via the strong-line calibrations by Storchi-Bergmann et al. (1998) and Carvalho et al. (2020) for a sample of 561 Seyfert nuclei in the local Universe ( $z \lesssim 0.31$ ) selected from the *Swift*-BAT 70-month AGN Data Release 2 (DR2) Catalog. These metallicities and the hard X-ray ( $\gtrsim 10$  keV) luminosities were used to study the  $L_X$ - $Z_{\text{NLR}}$  relation for the first time in Seyfert galaxies. We also studied the relation between the metallicities and the AGN properties. The physical properties comparison between Sy 1s and Sy 2s indicate that even in the narrow line regions of both AGN classes, Sy 1 still exhibit higher electron density in comparison to Sy 2. We found that the AGN metallicities are related to the hosts stellar masses following a downward redshift evolution, similar to that of SF galaxies, from lower to higher redshifts, but with lower values of O/H abundances (with a mean difference of 0.2–0.5 dex) in AGN hosts than in SF galaxies. We also found that the metallicities decrease with increasing X-ray luminosities and have significant correlations with  $\lambda_{\text{Edd}}$  at the redshift range  $z \lesssim 0.02$  (the overall oxygen and nitrogen dependent:  $r \sim -0.50 \pm 0.06$ ,  $p < 10^{-5}$ ,  $\sigma = 0.20$  dex) and at the full redshift range  $z \lesssim 0.31$  (oxygen dependent:  $r \sim -0.42 \pm 0.04$ ,  $p < 10^{-5}$ ,  $\sigma = 0.12$  dex and nitrogen dependent:  $r \sim -0.45 \pm 0.04$ ,  $p < 10^{-5}$ ,  $\sigma = 0.18$  dex). We argue that, these anticorrelations are driven by the X-ray luminosities, and they change with redshift, indicating that the AGNs are somehow driving the chemical enrichment of their host galaxies, as a result of the inflow of pristine gases that are diluting the metal-rich gases, together with a recent cessations on the star formation.

## ACKNOWLEDGEMENTS

We thank the anonymous referee for insightful comments and suggestions. MA gratefully acknowledges support from Coordenação de

Aperfeiçoamento de Pessoal de Nível Superior (CAPES). RR thanks Conselho Nacional de Desenvolvimento Científico e Tecnológico (CNPq, Proj. 311223/2020-6, 304927/2017-1, and 400352/2016-8), Fundação de amparo à pesquisa do Rio Grande do Sul (FAPERGS, Proj. 16/2551-0000251-7 and 19/1750-2), Coordenação de Aperfeiçoamento de Pessoal de Nível Superior (CAPES, Proj. 0001). OLD is grateful to the Fundação de Amparo à Pesquisa do Estado de São Paulo (FAPESP) and to Conselho Nacional de Desenvolvimento Científico e Tecnológico (CNPq) for the financial support. BT acknowledges support from the European Research Council (ERC) under the European Union’s Horizon 2020 research and innovation program (grant agreement 950533) and from the Israel Science Foundation (grant 1849/19). MV acknowledges support from grant ‘ESTANCIAS POSDOCTORALES POR MÉXICO 2022’ by CONACYT. CR acknowledges support from the Fondecyt Iniciación grant 11190831 and ANID BASAL project FB210003.

KO acknowledges support from the Korea Astronomy and Space Science Institute under the R&D program (Project No. 2023-1-830-01) supervised by the Ministry of Science and ICT and from the National Research Foundation of Korea (NRF- 2020R1C1C1005462).

## 6 DATA AVAILABILITY

The data underlying this article will be shared on reasonable request with the corresponding author.

## REFERENCES

- Abazajian K. N. et al., 2009, *ApJS*, 182, 543  
 Agostino C. J. et al., 2021, *ApJ*, 922, 156  
 Aguado D. S. et al., 2019, *ApJS*, 240, 23  
 Allende Prieto C., Lambert D. L., Asplund M., 2001, *ApJ*, 556, L63  
 Ananna T. T. et al., 2022, *ApJS*, 261, 9  
 Antonucci R., 1993, *ARA&A*, 31, 473  
 Armah M. et al., 2021, *MNRAS*, 508, 371  
 Audibert A., Riffel R., Sales D. A., Pastoriza M. G., Ruschel-Dutra D., 2017, *MNRAS*, 464, 2139  
 Baldwin J. A., Phillips M. M., Terlevich R., 1981, *PASP*, 93, 5  
 Baldwin J. A., Ferland G. J., Korista K. T., Hamann F., Dietrich M., 2003a, *ApJ*, 582, 590  
 Baldwin J. A., Hamann F., Korista K. T., Ferland G. J., Dietrich M., Warner C., 2003b, *ApJ*, 583, 649  
 Baumgartner W. H., Tueller J., Markwardt C. B., Skinner G. K., Barthelmy S., Mushotzky R. F., Evans P. A., Gehrels N., 2013, *ApJS*, 207, 19  
 Bennert N., Jungwiert B., Komossa S., Haas M., Chini R., 2006a, *A&A*, 456, 953  
 Bennert N., Jungwiert B., Komossa S., Haas M., Chini R., 2006b, *A&A*, 459, 55  
 Bentz M. C., Hall P. B., Osmer P. S., 2004, *AJ*, 128, 561  
 Berg D. A., Pogge R. W., Skillman E. D., Croxall K. V., Moustakas J., Rogers N. S. J., Sun J., 2020, *ApJ*, 893, 96  
 Berney S. et al., 2015, *MNRAS*, 454, 3622  
 Bian F., Kewley L. J., Dopita M. A., Blanc G. A., 2017, *ApJ*, 834, 51  
 Bieri R., Dubois Y., Silk J., Mamon G. A., Gaibler V., 2016, *MNRAS*, 455, 4166  
 Blanc G. A., Kewley L., Vogt F. P. A., Dopita M. A., 2015, *ApJ*, 798, 99  
 Boardman N. et al., 2022, *MNRAS*, 514, 2298  
 Bowen I. S., 1960, *ApJ*, 132, 1  
 Brownson S., Belfiore F., Maiolino R., Lin L., Carniani S., 2020, *MNRAS*, 498, L66  
 Cardelli J. A., Clayton G. C., Mathis J. S., 1989, *ApJ*, 345, 245  
 Carvalho S. P. et al., 2020, *MNRAS*, 492, 5675  
 Castro C. S., Dors O. L., Cardaci M. V., Hägele G. F., 2017, *MNRAS*, 467, 1507

- Cerqueira-Campos F. C., Rodríguez-Ardila A., Riffel R., Marinello M., Prieto A., Dahmer-Hahn L. G., 2021, *MNRAS*, 500, 2666
- Chen J. et al., 2019, *MNRAS*, 489, 855
- Cicone C. et al., 2014, *A&A*, 562, A21
- Cid Fernandes R., Stasińska G., Schlickmann M. S., Mateus A., Vale Asari N., Schoenell W., Sodré L., 2010, *MNRAS*, 403, 1036
- Clemens J. C., Crain J. A., Anderson R., 2004, in Moorwood A. F. M., Iye M., eds, *SPIE Conf. Ser. Vol. 5492, Ground-based Instrumentation for Astronomy*. SPIE, Bellingham, p. 331
- Congiu E. et al., 2017, *MNRAS*, 471, 562
- Curti M., Cresci G., Mannucci F., Marconi A., Maiolino R., Esposito S., 2017, *MNRAS*, 465, 1384
- Curti M., Mannucci F., Cresci G., Maiolino R., 2020, *MNRAS*, 491, 944
- Davies R. et al., 2020, *MNRAS*, 498, 4150
- Davison A., Hinkley D., 1997, Technical report, *Bootstrap Methods and Their Application*. Cambridge Univ. Press, Cambridge
- Dempsey R., Zakamska N. L., 2018, *MNRAS*, 477, 4615
- Denicoló G., Terlevich R., Terlevich E., 2002, *MNRAS*, 330, 69
- Díaz Á. I., Terlevich E., Castellanos M., Hägele G. F., 2007, *MNRAS*, 382, 251
- do Nascimento J. C. et al., 2022, *MNRAS*, 513, 807
- Dors O. L., 2021, *MNRAS*, 507, 466
- Dors O. L. J., Storchi-Bergmann T., Riffel R. A., Schimdt A. A., 2008, *A&A*, 482, 59
- Dors O. L., Cardaci M. V., Hägele G. F., Krabbe Á. C., 2014, *MNRAS*, 443, 1291
- Dors O. L., Monteiro A. F., Cardaci M. V., Hägele G. F., Krabbe A. C., 2019, *MNRAS*, 486, 5853
- Dors O. L. et al., 2020a, *MNRAS*, 492, 468
- Dors O. L., Maiolino R., Cardaci M. V., Hägele G. F., Krabbe A. C., Pérez-Montero E., Armah M., 2020b, *MNRAS*, 496, 3209
- Dors O. L. et al., 2022, *MNRAS*, 514, 5506
- El-Badry K., Wetzel A., Geha M., Hopkins P. F., Kereš D., Chan T. K., Faucher-Giguère C.-A., 2016, *ApJ*, 820, 131
- Elbaz D., Jahnke K., Pantin E., Le Borgne D., Letawe G., 2009, *A&A*, 507, 1359
- Fabian A. C., 2012, *ARA&A*, 50, 455
- Feltre A., Charlot S., Gutkin J., 2016, *MNRAS*, 456, 3354
- Ferland G. J., Netzer H., 1983, *ApJ*, 264, 105
- Ferland G. J. et al., 2017, *Rev. Mex. Astron. Astrofís.*, 53, 385
- Freitas I. C. et al., 2018, *MNRAS*, 476, 2760
- Gallagher R., Maiolino R., Belfiore F., Drory N., Riffel R., Riffel R. A., 2019, *MNRAS*, 485, 3409
- Garnica K., Negrete C. A., Marziani P., Dultzin D., Śniegowska M., Panda S., 2022, *A&A*, 667, A105
- Gaskell C. M., 1982, *PASP*, 94, 891
- Gaskell C. M., 1984, *Astrophys. Lett.*, 24, 43
- Gaskell C. M., Ferland G. J., 1984, *PASP*, 96, 393
- Gehrels N. et al., 2004, *ApJ*, 611, 1005
- Graham A. W., 2016, in Laurikainen E., Peletier R., Gadotti D., eds, *Galaxy Bulges and Their Massive Black Holes: A Review*. Galactic Bulges, Astrophysics and Space Science Library, Vol. 418, Springer, Cham, Switzerland
- Granato G. L., De Zotti G., Silva L., Bressan A., Danese L., 2004, *ApJ*, 600, 580
- Hägele G. F., Díaz Á. I., Terlevich E., Terlevich R., Pérez-Montero E., Cardaci M. V., 2008, *MNRAS*, 383, 209
- Halpern J. P., 1982, PhD thesis, Harvard University, Cambridge, MA
- Halpern J. P., Steiner J. E., 1983, *ApJ*, 269, L37
- Hamann F., Ferland G., 1993, *ApJ*, 418, 11
- Heckman T. M., Miley G. K., van Breugel W. J. M., Butcher H. R., 1981, *ApJ*, 247, 403
- Ho L. C., 2008, *ARA&A*, 46, 475
- Hopkins P. F., 2012, *MNRAS*, 420, L8
- Hopkins P. F., Elvis M., 2010, *MNRAS*, 401, 7
- Horne K. et al., 2021, *ApJ*, 907, 76
- Huang C. et al., 2019, *ApJ*, 886, 31
- Ishibashi W., Fabian A. C., 2012, *MNRAS*, 427, 2998
- Jensen E. B., Strom K. M., Strom S. E., 1976, *ApJ*, 209, 748
- Ji X., Yan R., Riffel R., Drory N., Zhang K., 2020, *MNRAS*, 496, 1262
- Jiang T., Malhotra S., Rhoads J. E., Yang H., 2019, *ApJ*, 872, 145
- Kakkad D. et al., 2018, *A&A*, 618, A6
- Kakkad D. et al., 2022, *MNRAS*, 511, 2105
- Kaspi S., Smith P. S., Netzer H., Maoz D., Jannuzi B. T., Giveon U., 2000, *ApJ*, 533, 631
- Kawamuro T., Ricci C., Izumi T., Imanishi M., Baba S., Nguyen D. D., Onishi K., 2021, *ApJS*, 257, 64
- Kennicutt Robert C. J., Bresolin F., Garnett D. R., 2003, *ApJ*, 591, 801
- Kewley L. J., Ellison S. L., 2008, *ApJ*, 681, 1183
- Kewley L. J., Dopita M. A., Sutherland R. S., Heisler C. A., Trevena J., 2001, *ApJ*, 556, 121
- Kewley L. J., Jansen R. A., Geller M. J., 2005, *PASP*, 117, 227
- Kewley L. J., Groves B., Kauffmann G., Heckman T., 2006, *MNRAS*, 372, 961
- King A., Pounds K., 2015, *ARA&A*, 53, 115
- Kobulnicky H. A., Kewley L. J., 2004, *ApJ*, 617, 240
- Kormendy J., Ho L. C., 2013, *ARA&A*, 51, 511
- Koss M. J. et al., 2016, *ApJ*, 825, 85
- Koss M. et al., 2017, *ApJ*, 850, 74
- Koss M. J. et al., 2021, *ApJS*, 252, 29
- Koss M. J. et al., 2022a, *ApJS*, 261, 2
- Koss M. J. et al., 2022b, *ApJS*, 261, 6
- Kraemer S. B., Wu C.-C., Crenshaw D. M., Harrington J. P., 1994, *ApJ*, 435, 171
- Lamperti I. et al., 2017, *MNRAS*, 467, 540
- Landt H. et al., 2019, *MNRAS*, 489, 1572
- Lilly S. J., Carollo C. M., Pipino A., Renzini A., Peng Y., 2013, *ApJ*, 772, 119
- Liu T. et al., 2020, *ApJ*, 896, 122
- Lopez-Sanchez A. R., Esteban C., 2010, preprint ([arXiv:1004.5251](https://arxiv.org/abs/1004.5251))
- Lu K.-X., Zhao Y., Bai J.-M., Fan X.-L., 2019, *MNRAS*, 483, 1722
- Luridiana V., Morisset C., Shaw R. A., 2015, *A&A*, 573, A42
- Maiolino R. et al., 2008, *A&A*, 488, 463
- Maiolino R. et al., 2017, *Nature*, 544, 202
- Marino R. A. et al., 2013, *A&A*, 559, A114
- Matsuoka K., Nagao T., Maiolino R., Marconi A., Taniguchi Y., 2009, *A&A*, 503, 721
- Matsuoka K., Nagao T., Marconi A., Maiolino R., Taniguchi Y., 2011, *A&A*, 527, A100
- Matsuoka K., Nagao T., Marconi A., Maiolino R., Mannucci F., Cresci G., Terao K., Ikeda H., 2018, *A&A*, 616, L4
- Mejía-Restrepo J. E., Trakhtenbrot B., Lira P., Netzer H., Capellupo D. M., 2016, *MNRAS*, 460, 187
- Mingozzi M. et al., 2019, *A&A*, 622, A146
- Monteiro A. F., Dors O. L., 2021, *MNRAS*, 508, 3023
- Moore C. E., 1945, *Contributions from the Princeton University Observatory*, 20, 1
- Nagao T., Maiolino R., Marconi A., 2006, *A&A*, 447, 863
- Nayakshin S., Zubovas K., 2012, *MNRAS*, 427, 372
- Netzer H., Shemmer O., Maiolino R., Oliva E., Croom S., Corbett E., di Fabrizio L., 2004, *ApJ*, 614, 558
- Nicholls D. C., Kewley L. J., Sutherland R. S., 2020, *PASP*, 132, 033001
- Oh K. et al., 2017, *MNRAS*, 464, 1466
- Oh K., Ueda Y., Akiyama M., Suh H., Koss M. J., Kashino D., Hasinger G., 2019, *ApJ*, 880, 112
- Oh K. et al., 2022, *ApJS*, 261, 4
- Oke J. B. et al., 1995, *PASP*, 107, 375
- Osterbrock D. E., 1981, *ApJ*, 249, 462
- Osterbrock D. E., 1989, *Astrophysics of Gaseous Nebulae and Active Galactic Nuclei*. University Science Books, Sausalito, California, USA
- Osterbrock D. E., Ferland G. J., 2006, *Astrophysics of Gaseous Nebulae and Active Galactic Nuclei*. University Science Books, Sausalito, California, USA
- Owen A. B., 2007, *Contemp. Math.*, 443, 59
- Pagel B. E. J., Edmunds M. G., Blackwell D. E., Chun M. S., Smith G., 1979, *MNRAS*, 189, 95



- Peimbert M., Peimbert A., Delgado-Inglada G., 2017, *PASP*, 129, 082001
- Pérez-Montero E., 2017, *PASP*, 129, 043001
- Peterson B. M. et al., 2013, *ApJ*, 779, 109
- Pilyugin L. S., 2003, *A&A*, 399, 1003
- Pilyugin L. S., Grebel E. K., 2016, *MNRAS*, 457, 3678
- Pistis F. et al., 2022, *A&A*, 663, A162
- Rees M. J., 1989, *MNRAS*, 239, 1P
- Revalski M., Crenshaw D. M., Kraemer, 2018, *ApJ*, 856, 46
- Ricci C., Ueda Y., Koss M. J., Trakhtenbrot B., Bauer F. E., Gandhi P., 2015, *ApJ*, 815, L13
- Ricci C. et al., 2017a, *ApJS*, 233, 17
- Ricci C. et al., 2017b, *Nature*, 549, 488
- Ricci C. et al., 2018, *MNRAS*, 480, 1819
- Ricci C. et al., 2022, *ApJ*, 938, 67
- Riffel R. et al., 2021, *MNRAS*, 501, 4064
- Riffel R. et al., 2022, *MNRAS*, 512, 3906
- Rojas A. F. et al., 2020, *MNRAS*, 491, 5867
- Salomé Q., Salomé P., Miville-Deschênes M. A., Combes F., Hamer S., 2017, *A&A*, 608, A98
- Sanders R. L. et al., 2016, *ApJ*, 816, 23
- Sanders R. L. et al., 2021, *ApJ*, 914, 19
- Schawinski K., Thomas D., Sarzi M., Maraston C., Kaviraj S., Joo S.-J., Yi S. K., Silk J., 2007, *MNRAS*, 382, 1415
- Schnorr-Müller A. et al., 2016, *MNRAS*, 462, 3570
- Sergeev S. G., Nazarov S. V., Borman G. A., 2017, *MNRAS*, 465, 1898
- Shemmer O., Netzer H., Maiolino R., Oliva E., Croom S., Corbett E., di Fabrizio L., 2004, *ApJ*, 614, 547
- Shimizu T. T. et al., 2019, *MNRAS*, 490, 5860
- Silk J., 2013, *ApJ*, 772, 112
- Smith K. L., Koss M., Mushotzky R., Wong O. I., Shimizu T. T., Ricci C., Ricci F., 2020, *ApJ*, 904, 83
- Somerville R. S., Davé R., 2015, *ARA&A*, 53, 51
- Springel V., Di Matteo T., Hernquist L., 2005, *MNRAS*, 361, 776
- Stanley F., Harrison C. M., Alexander D. M., Swinbank A. M., Aird J. A., Del Moro A., Hickox R. C., Mullaney J. R., 2015, *MNRAS*, 453, 591
- Storchi-Bergmann T., Calzetti D., Kinney A. L., 1994, *ApJ*, 429, 572
- Storchi-Bergmann T., Schmitt H. R., Calzetti D., Kinney A. L., 1998, *AJ*, 115, 909
- Suganuma M. et al., 2006, *ApJ*, 639, 46
- Suh H. et al., 2019, *ApJ*, 872, 168
- Sun A.-L. et al., 2018, *MNRAS*, 480, 2302
- Tang J.-J. et al., 2019, *MNRAS*, 484, 2575
- Temple M. J., Ferland G. J., Rankine A. L., Chatzikos M., Hewett P. C., 2021, *MNRAS*, 505, 3247
- Thomas A. D., Kewley L. J., Dopita M. A., Groves B. A., Hopkins A. M., Sutherland R. S., 2019, *ApJ*, 874, 100
- Toribio San Cipriano L., Domínguez-Guzmán G., Esteban C., García-Rojas J., Mesa-Delgado A., Bresolin F., Rodríguez M., Simón-Díaz S., 2017, *MNRAS*, 467, 3759
- Trakhtenbrot B. et al., 2017, *MNRAS*, 470, 800
- Tremonti C. A. et al., 2004, *ApJ*, 613, 898
- Trussler J., Maiolino R., Maraston C., Peng Y., Thomas D., Goddard D., Lian J., 2020, *MNRAS*, 491, 5406
- van Zee L., Salzer J. J., Haynes M. P., O'Donoghue A. A., Balonek T. J., 1998, *AJ*, 116, 2805
- Vaona L., Ciroi S., Di Mille F., Cracco V., La Mura G., Rafanelli P., 2012, *MNRAS*, 427, 1266
- Veilleux S., Osterbrock D. E., 1987, *ApJS*, 63, 295
- Vernet J. et al., 2011, *A&A*, 536, A105
- Wada K., Yonekura K., Nagao T., 2018, *ApJ*, 867, 49
- Wang X., Loeb A., 2018, *New Astronomy*, 61, 95
- Wang J.-M., Yan C.-S., Gao H.-Q., Hu C., Li Y.-R., Zhang S., 2010, *ApJ*, 719, L148
- Wysota A., Gaskell C. M., 1988. in Miller H.R., Wiita P. J., eds, Reddening of narrow line regions. Active Galactic Nuclei. Lecture Notes in Physics, Vol. 307, Springer, Berlin, Heidelberg
- Xu F., Bian F., Shen Y., Zuo W., Fan X., Zhu Z., 2018, *MNRAS*, 480, 345
- York D. G. et al., 2000, *AJ*, 120, 1579
- Zhang X.-G., Feng L.-L., 2016, *MNRAS*, 457, L64
- Zou F., Yang G., Brandt W. N., Xue Y., 2019, *ApJ*, 878, 11
- Zubovas K., Bourne M. A., 2017, *MNRAS*, 468, 4956
- Zubovas K., Nayakshin S., King A., Wilkinson M., 2013, *MNRAS*, 433, 3079

This paper has been typeset from a  $\text{\TeX}/\text{\LaTeX}$  file prepared by the author.